

This is to certify that the dissertation entitled

Methods to Identify Intermittent Electrical and Mechanical Faults in Permanent Magnet AC Drives Based on Time-Frequency Analysis

presented by

Wesley G. Zanardelli

has been accepted towards fulfillment of the requirements for the

Ph.D. degree in Electrical Engineering

Major Professor's Signature

11 Nov 05

Date

MSU is an Affirmative Action/Equal Opportunity Institution

LIBRARY Michigan State University

PLACE IN RETURN BOX to remove this checkout from your record. TO AVOID FINES return on or before date due. MAY BE RECALLED with earlier due date if requested.

DATE DUE	DATE DUE	DATE DUE
06±130 & 2000		

2/05 p:/CIRC/DateDue.indd-p.1

Methods to Identify Intermittent Electrical and Mechanical Faults in Permanent Magnet AC Drives Based on Time-Frequency Analysis

By

Wesley G. Zanardelli

A DISSERTATION

Submitted to

Michigan State University
in partial fulfillment of the requirements
for the degree of

DOCTOR OF PHILOSOPHY

Department of Electrical and Computer Engineering

ABSTRACT

Methods to Identify Intermittent Electrical and Mechanical Faults in Permanent Magnet AC Drives Based on Time-Frequency Analysis

By

Wesley G. Zanardelli

Prognosis of failures of electric drives can be achieved through the detection of non-catastrophic conditions, recognized as faults. As the frequency and severity of these faults increase, the expected working life of the drive decreases, leading to eventual failure. The goal of this work is to develop new techniques which can detect and classify conditions in electric drives which lead to failure. In this work, methods are presented to identify developing electrical and mechanical faults based on both Fourier and wavelet analysis of the field oriented currents in PMAC drives. Linear discriminant analysis is used to classify between the fault types. This dissertation includes a survey of diagnostic approaches used for various machine types. The experimental setup and results from testing are included.

Copyright © by Wesley G. Zanardelli 2005 To my parents, Virgil and Loretta Zanardelli

ACKNOWLEDGMENTS

I would like to express my gratitude and thanks to my advisor Professor Elias Strangas for his guidance, support, and his professional as well as personal example. I would also like to thank Professors Selin Aviyente, Michael Frazier, and Feng Peng for their time and effort in being part of my committee.

I would like to extend special thanks to those at Delphi Corporation who helped make this research possible. I would like to thank Nady Boules, Linos Jacovides, and Christian Ross for providing the funding for this work. I would also like to thank Sayeed Mir, Tomy Sebastian, Mohammad Islam, Avoki Omekanda, Bruno Lequesne, and Tom Nehl for their technical guidance throughout this work.

Special words of thanks go to my lab colleagues John Kelly, Sinisa Jurkovic, and Eric Thomas for all of their support. I would also like to thank Jin Wang and Alan Joseph from the MSU Power Electronics and Motor Drives Laboratory. I would like to thank Arthur Matteson whose year-long commitment resulted in the I/O board used in the experimental setup. I would also like to thank the members of the department whose help was much appreciated, including Brian Wright, Roxanne Peacock, Vanessa Mitchner, and Pauline Van Dyke.

Finally, I owe special thanks to my parents, Virgil and Loretta Zanardelli, whose support and encouragement helped make my graduate studies possible.

TABLE OF CONTENTS

LI	ST C	F TABLES	ix								
LI	ST C	F FIGURES	x								
1 Introduction											
	1.1	Literature Review	3								
		1.1.1 Methods to Detect Electrical Faults	3								
		1.1.2 Methods to Detect Mechanical Faults	10								
		1.1.3 Methods to Detect Both Electrical and Mechanical Faults	13								
		1.1.4 Methods to Detect Arcing Faults	15								
		1.1.5 Methods to Mitigate Faults	17								
2	The	ory	19								
	2.1	Fast Fourier Transform	19								
	2.2	Short-Time Fourier Transform	20								
	2.3	Discrete Wavelet Transform	21								
	2.4	Filter Banks	25								
	2.5	Undecimated Discrete Wavelet Transform	27								
	2.6	Energy Calculations	29								
	2.7	Categorization	30								
		2.7.1 Nearest Neighbor Rule	33								
		2.7.2 Linear Discriminant Analysis	34								
	2.8	Cross Validation	35								
	2.9	PMSM Torque Control	36								
	2.10	Discrete-Time PI Controller	37								
3	App	lications	39								
	3.1	Electrical Drive Faults	40								
		3.1.1 Intermittent Increased Contact Resistance	41								
		3.1.2 Turn-Terminal Short	41								
	3.2	Mechanical Drive Faults	42								

	•	Methods and Results
4.1		ion and Classification Methods
	4.1.1	Algorithm Based on the FFT Applied to Electrical Faults (Slow
	410	Controller Response)
	4.1.2	Algorithm Based on the STFT Applied to Electrical Faults
	410	(Slow Controller Response)
	4.1.3	Algorithm Based on the STFT Applied to Electrical Faults
	4.1.4	(Fast Controller Response)
	4.1.4	Separate Classification of Fault Inception and Clearing (Slow
		Controller Response)
	4.1.5	Algorithm Based on the STFT Applied to Electrical Faults with
	4.1.U	Separate Classification of Fault Inception and Clearing (Fast
		Controller Response)
	4.1.6	Algorithm Based on the STFT Applied to Mechanical Faults
		(Fast Controller Response)
	4.1.7	Algorithm Based on the DWT
	4.1.8	Algorithm Based on the UDWT Applied to Electrical Faults
		(Slow Controller Response)
	4.1.9	Algorithm Based on the UDWT Applied to Electrical Faults
		(Fast Controller Response)
	4.1.10	Algorithm Based on the UDWT Applied to Electrical Faults
		with Separate Classification of Fault Inception and Clearing
		(Slow Controller Response)
	4.1.11	Algorithm Based on the UDWT Applied to Electrical Faults
		with Separate Classification of Fault Inception and Clearing
		(Fast Controller Response)
	4.1.12	Algorithm Based on the UDWT Applied to Mechanical Faults
		(Fast Controller Response)
4.2	Finite	Element Analysis
	4.2.1	Time Step
	4.2.2	Current Sources vs. Voltage Sources
	4.2.3	Measurement Resistors

	5.2	Xilinx I/O Board	84
		5.2.1 Inverter	85
	5.3	Sensor Board	86
	5.4	Shaft Encoder	86
	5.5	Dynamometer	86
	5.6	Electronic Switch Board	88
	5.7	Mechanical Gearbox	91
6	Cor	nclusions	93
В	IBLI	OGRAPHY	er 85 86 er 86 er 86 vitch Board 88 Gearbox 91

LIST OF TABLES

4.1	Algorithm	Performance	(Section	4.1.2)	•										50
4.2	Algorithm	Performance	(Section	4.1.3)				•							52
4.3	Algorithm	Performance	(Section	4.1.4)											55
4.4	Algorithm	Performance	(Section	4.1.5)											58
4.5	${\bf Algorithm}$	Performance	(Section	4.1.6)							•				60
4.6	${\bf Algorithm}$	Performance	(Section	4.1.8)											64
4.7	${\bf Algorithm}$	Performance	(Section	4.1.9)											67
4.8	${\bf Algorithm}$	${\bf Performance}$	$({\bf Section}$	4.1.10)											70
4.9	${\bf Algorithm}$	Performance	(Section	4.1.11)											72
4.10	Algorithm	Performance	(Section	4.1.12)									_	_	75

LIST OF FIGURES

Effect of Various Faults on the Park's Vector Pattern ($\omega = 2$) [10]	8
Effect of Various Faults on the Park's Vector Pattern ($\omega=4$) [10]	9
Temporal Coincidence of DWT Coefficients Corresponding to an Event	10
Characteristic Ratings of Fault Tolerant Inverter Topologies	18
FFT Tiling	19
STFT Tiling	20
STFT Block Diagram	21
DWT Tiling	21
Scaling Function and Wavelet Vector Spaces	24
Haar Scaling and Wavelet Functions	24
Two-Stage Filter Bank Analysis Tree	26
UDWT Filters Modified by the "Algorithme à Trous"	27
Example of Shift-Invariance of the UDWT	28
Example DWT Showing Coefficient Indices	29
Vector-Controlled PMSM Drive	36
PI Controller	38
Experimental Mimic of Series Resistance Fault	41
Turn-Terminal Short Stator Modifications	43
Test Gears	44
Typical Results (Section 4.1.1)	47
Typical Results (Section 4.1.2)	49
Typical Results (Section 4.1.3)	52
Typical Results (Section 4.1.4)	54
Typical Results (Section 4.1.5)	57
Experimental Results (Section 4.1.6)	59
Original Signal	61
DWT of the Original Signal	62
Energy in the DWT of the Original Signal	62
	Effect of Various Faults on the Park's Vector Pattern $(\omega=4)$ [10] . Temporal Coincidence of DWT Coefficients Corresponding to an Event Characteristic Ratings of Fault Tolerant Inverter Topologies

4.10	Typical Results (Section 4.1.8)	63
4.11	Typical Results (Section 4.1.9)	66
4.12	Typical Results (Section 4.1.10)	69
4.13	Typical Results (Section 4.1.11)	72
4.14	Experimental Results (Section 4.1.12)	74
5.1	Experimental Setup Block Diagram	79
5.2	Electronic Switch	80
5.3	Motor / Dynamometer / Encoder Fixture	81
5.4	Motor / Dynamometer Shaft Coupling	82
5.5	Motor / Dynamometer Solid Shaft Coupling	83
5.6	Motor / Encoder Interface	83
5.7	Mechanical Gearbox Experimental Setup	84
5.8	Xilinx and Xilinx I/O Boards	85
5.9	Current and Voltage Sensor Board	87
5.10	Dynamometer Torque-Speed Characteristics	88
5.11	Electronic Switch Board Schematic	89
5.12	Electronic Switch Board Layout	90
5.13	Gear Box Block Diagram	91
5.14	Gear Illustration	92

CHAPTER 1

Introduction

Reliability of electrical machines and drives is an area of increased attention and research. Diagnosing correctly a failure in an electrical drive can lead to mitigation and continued operation, albeit at reduced power levels.

On the other hand, prior to failure the drive can intermittently show signs of a developing fault, while it is operating normally. Detecting these early signs can lead to appropriate actions before a failure occurs. For the remainder of this paper the term fault is defined as a condition of the drive that allows for continued operation, but may eventually lead to failure.

In this work, methods to identify intermittent stator winding and gear faults in PMAC drives are developed. The faults of interest are non-catastrophic, meaning they allow for continued operation of the drive, but increase the likelihood of failure. Early detection of these faults can alert the operator to schedule maintenance of the drive before failure occurs. The work is based on the following considerations:

- 1. Many faults that correspond to a condition that may lead to a failure are intermittent in nature and correspond to transient phenomena. Such phenomena require non-stationary methods to be analyzed and detected.
- 2. Non-stationary methods are often sensitive to the sampling starting point.

3. The transients that are studied here are often very fast. Electrical transients in particular correspond to the distributed characteristics of windings, including parasitic capacitances. Simulating these transients requires very short time steps and detailed modeling, which is prohibitive when extensive data collection is needed.

Two types of electrical stator faults and one type of mechanical gear fault with varying degrees of severity are explored. The first electrical fault is a momentary increased resistance in one phase due to a bad connection between the motor and the controller. The second electrical fault is a turn-terminal short, simulating an insulation failure in the stator windings of the motor. The mechanical fault is missing gear teeth in a gearbox coupled to the motor. The methods introduced are designed to detect the short transients, which over time will develop into a fault, e.g. momentary increased resistance.

The algorithms presented are based on analysis of the Fast Fourier Transform (FFT), Short-Time Fourier Transform (STFT), Discrete Wavelet Transform (DWT), and the Undecimated Discrete Wavelet Transform (UDWT) of the torque producing component of the field oriented stator currents. Thresholding on the energy in the analysis coefficients is used to detect a fault in the machine, and linear discriminant analysis is used to classify between the fault types.

A collection of observed data is used to train the detection and classification components of the algorithm. Results obtained using both Finite Element Analysis (FEA) and simulation were considered for use in algorithm development, however, while these techniques can be used to approximate the effect of a fault, it is not possible to model all of the dynamics in an electric drive coupled to a load. Results obtained from laboratory experiments proved to be more useful.

The algorithms developed can be implemented in an online system, using extra processing time in the motor controller.

1.1 Literature Review

1.1.1 Methods to Detect Electrical Faults

In [1], a method to detect turn-turn insulation failures in induction machines was described. The line-neutral stator voltages were measured and filtered to remove the fundamental component of the machine excitation voltage. The RMS value of $v_{sum} = v_{an} + v_{bn} + v_{cn}$ of the filtered components is zero in a balanced machine, however in the case of turn-turn insulation failures, the number of shorted turns could be determined by the amplitude. This technique was implemented offline, and requires that the machine be star connected with the neutral accessible.

The Park's vector pattern of the currents is analyzed for stator voltage unbalance or an open phase in three-phase induction machines in [2]. The Park's vector pattern is plotted in the stationary frame of reference using a two-phase representation of the measured stator currents for one electrical cycle. The plot is analyzed using an Artificial Neural Network (ANN) to check for a stator voltage unbalance or an open phase. The occurrence of either of these faults manifests itself in the deformation of the current Park's vector pattern corresponding to a healthy condition. This deformation leads to an elliptic pattern, whose major axis orientation is associated with the faulty phase. The severity of the deformation helps to distinguish between the two faults, with the open phase fault the most deformed. A mathematical model of the induction motor is not required. This system is implemented offline.

Signal processing methods were used in [3] to analyze three-phase induction machines for the presence of broken rotor bars or end rings. An FFT is performed on the currents and a diagnostic index equal to the sum of the amplitude of the two sideband current components at $(1 \pm 2s)f$, where s is the slip of the machine, and f is the fundamental component of the current, is assigned. If the value of the diagnostic index exceeds a threshold, it is determined that either a broken rotor bar or end

ring is present. Knowledge of the main nameplate data of the machine as well as the number of bars is required for this system. This system is implemented offline.

The signal processing methods used in [4] were based on a Condition Monitoring Vector Database to find the presence of broken rotor bars in induction machines. First a set of Condition Monitoring Vectors (CMV) were determined through simulations using the time-stepping Finite Element (TSFE) technique, and a single vector was computed for each complete AC cycle, both in the presence and absence of a fault. The CMV is defined in (1.1),

$$CMV = \left[\frac{V_n}{V_p} \frac{I_n}{I_p} \frac{Z_n}{Z_p} A (f_{LSB}) \Delta \delta_{BB} \Delta \delta_{SC} \omega_m T_{dev} \right]$$
 (1.1)

where V, I, and Z with the subscripts n and p are the negative and positive sequence components of the stator voltages, currents, and associated impedances; $A(f_{LSB})$ is the amplitude of the low sideband frequency spectrum component of the stator current at the frequency $(1-2s)f_s$, where f_s is the power supply frequency; $\Delta \delta_{BB}$ and $\Delta \delta_{SC}$ represent the range of oscillation of the resultant mid air-gap magnet field for broken rotor bars and stator winding inter-turn faults; and ω_m and T_{dev} are the motor speed and developed motor torque respectively.

Finally, an artificial intelligence-based statistical machine learning approach, using Gaussian Mixture Models, was used to train a Bayesian maximum likelihood classifier. Experimental results showed that the algorithm could discern between various numbers of broken rotor bars.

In [5], BLDC machines were analyzed using parameter estimation in a model-based technique. Based on the inverter supply voltage, the DC current, and the mechanical speed, a least-squares method was used to estimate parameters in a model of the machine. In the model for the electrical subsystem (1.2), estimates of R and k_E were

obtained.

$$\bar{v}(t) = R\bar{i}(t) + k_E \omega_r(t) \tag{1.2}$$

In the model for the mechanical subsystem (1.3), estimates for J, c_c , and c_v were obtained.

$$J\dot{\omega}_r(t) = k_T \bar{i} - c_c \operatorname{sign}(\omega_r(t)) - c_v \omega_r(t)$$
(1.3)

Here, c_c is the Coulomb friction coefficient, c_v is the viscose friction coefficient, and it is assumed that $k_T = k_E$. From the electrical model, the authors could determine whether the phase resistance of all coils had increased, indicating an increase in stator temperature, or a broken coil. From the mechanical model, the authors could detect increases in Coulomb and viscose friction.

Permanent magnet brush DC machines are analyzed for the presence of an open phase / broken connector fault, shorting of adjacent commutator bars, and worn brush faults in [6]. This approach is model-based and uses block-pulse function series techniques to estimate parameters in a continuous-time system. This is advantageous as it eliminates the need to discretize the system so that an algorithm like the least-squares method can be used. Based on measured DC current, DC voltage, and mechanical angular velocity, estimates of the armature resistance and inductance, back-EMF coefficient, rotor inertia, and friction coefficient are obtained from the motor model. These parameters are passed to an ANN to determine the fault type. This system was implemented offline.

Support Vector Machine (SVM) based classification, [7], was used in [8] to classify between faults in induction machines. SVMs are used to map a set of coefficients to a high-dimensional feature space where a set of 'best' separating hyperplanes are constructed. This mapping is based on a set of kernel functions, whose selection is critical. SVMs are binary classifiers, and hence, for multiclass problems, either one-against-all or one-against-one classifiers are developed. In this work, the one-

against-one formulation was used requiring n(n-1)/2 classifiers, e.g. for 6 faults (and healthy), 21 classifiers would be required.

Stator line currents, circulating currents between parallel stator branches and forces between the stator and rotor were analyzed. These quantities were computed using FEA and noise was added to them (0 mean, 3% variance of the amplitude of the current). The power spectrum of each signal was used for classification. Faults analyzed included shorted turns, shorted coils, broken rotor bars, broken end rings, rotor eccentricities, and asymmetrical line voltages. Analysis was performed for both 35kW and 1600kW induction motors.

Simulation results showed that classification of faults based on any of the above parameters was possible. Experimental results showed that classification of faults based on stator line currents was possible only when the measurement data was used for both training and testing of the classifier.

FEA (Flux2D) was used in [9] to determine the fault signatures in the DC bus voltage and current, stator currents, torque, and speed in a trapezoidal BLDC machine. The following faults were studied: Single-phase open circuit fault; phase-to-phase terminal short circuit; and internal turn-to-turn short circuit (across 6/26 turns of one coil). The machine was a 3-phase, 6 pole, 18 slot machine with a bifurcated stator tooth structure (helping to reduce torque ripple and doubling the frequency of cogging). The rotor of the machine had 6 Nd-Fe-B magnet poles magnetized radially. Six-step / voltage mode control was used. In this type of control, each switching pattern lasts 60 electrical degrees, and with a 6-pole machine, 20 mechanical degrees. An experimental setup was used to validate the FEA model.

In the case of the single-phase open circuit fault, the speed of the machine decays to zero and commutation stops. A spark voltage is induced across the break as well. In the case of the phase-to-phase terminal short circuit, the mechanical response is similar to the single-phase open circuit fault, however the currents were found to

become unstable. Finally, in the case of the internal turn-to-turn short circuit, the torque and speed decrease a negligible amount (< 0.05%) and the change in the voltages and currents was also found to be negligible.

In [10], simulated faults were imposed on a 3-phase model of an interior permanent magnet motor under the assumptions of constant motor speed and constant current references. The faults investigated follow:

- Switch-on failure of one transistor;
- Switch-on failure of both the transistors of a leg;
- Switch-on failure of all the transistors of the inverter;
- Open circuit of one motor phase;
- Switch-off failure of one transistor;
- DC supply failure.

The effects of the various faults on the Park's vector pattern are shown in Fig. 1.1 for $\omega = 2$ and in Fig. 1.2 for $\omega = 4$. In the case of a healthy drive, the plot is essentially circular. Each fault listed above distorts the circular shape in a unique way. The plots are based on simulation results. This work is a starting point for detection and classification of faults as well as strategies for reconfiguring the drive and control techniques, although these topics are not discussed in this paper.

A model-based approach based on wavelet analysis to detect faults in induction motors is presented in [11]. Application of the wavelet transform helped to remove variations due to changes in speed. The temporal coincidence of wavelet coefficients at different scales corresponding to an event was discussed and is shown in Fig. 1.3.

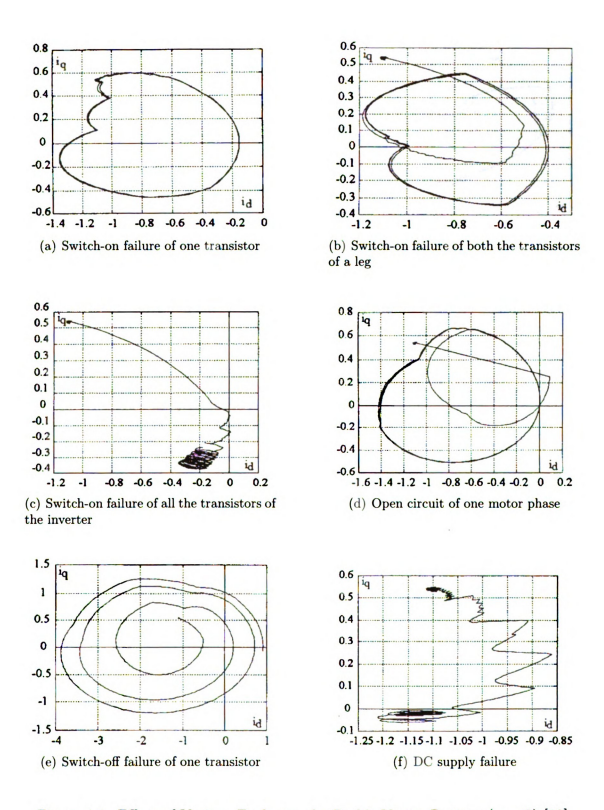


Figure 1.1. Effect of Various Faults on the Park's Vector Pattern ($\omega=2$) [10]

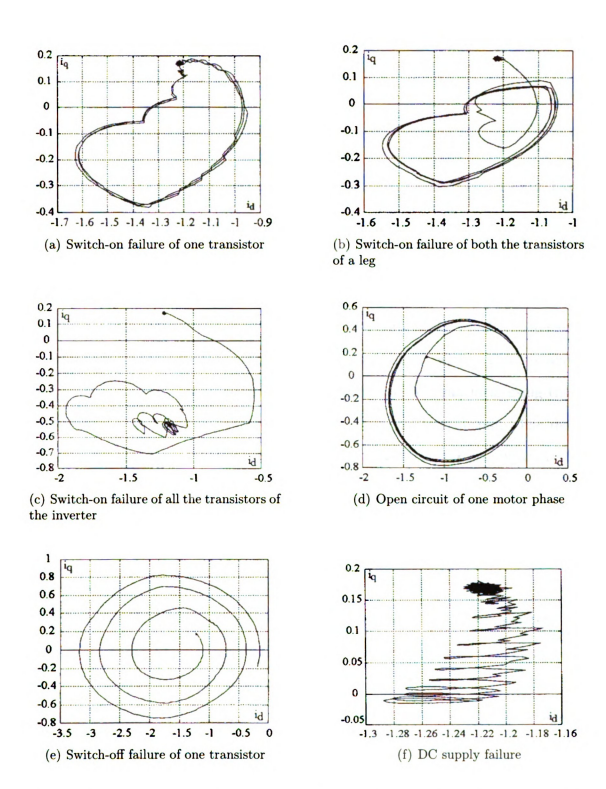


Figure 1.2. Effect of Various Faults on the Park's Vector Pattern ($\omega = 4$) [10]

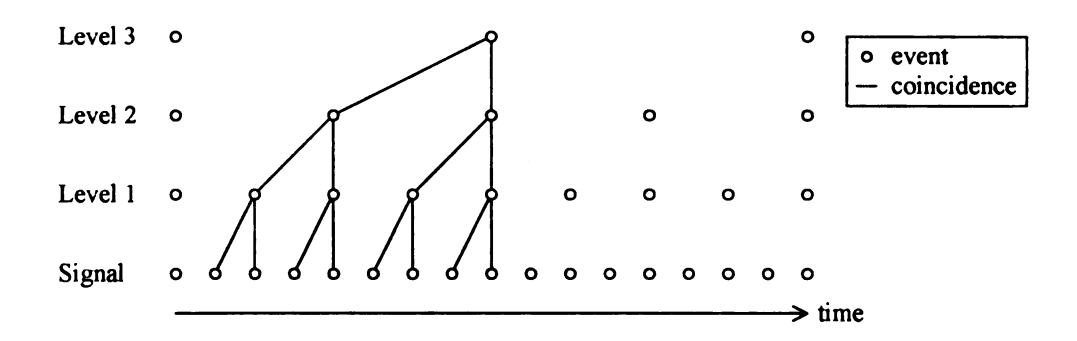


Figure 1.3. Temporal Coincidence of DWT Coefficients Corresponding to an Event

1.1.2 Methods to Detect Mechanical Faults

Signatures in the vibration of a machine are often used to detect mechanical faults. These techniques require the installation of an accelerometer, which can be bulky and adds to cost. In [12], a three phase induction machine with a gearbox and its corresponding bearing assemblies are analyzed. The wavelet transform using the D4 mother wavelet was applied to the FFT of the accelerometer output. The details coefficients at the first scale were the input to an ANN used for classification. The ANN was trained to detect faults including the presence of a small 'blip' of 2mm diameter welded onto a gear tooth, a triangle shaped area missing from a gear tooth, and a fractured inner race of the bearing housing. This technique is implemented offline.

FEA was used in [13] to calculate electromagnetic variables and parameters, used to detect mechanical faults in PMAC machines. These parameters were flux linkages and inductances as functions of rotor position, and were stored in a look-up table and then used in a transient simulation of the motor. This process was repeated for various rotor conditions. Faults were then directly mapped to the increase in harmonics. This technique detects the presence of static and dynamic eccentricities, and flux disturbances originating from defects to the permanent magnets.

The authors determined that the current harmonic components can be analyzed

in either the rotor or stationary reference frame. In the case of the static eccentricity, however, analysis in the stationary reference frame was required, since the fault effects in the rotor reference frame were obscured.

A set of wavelets were introduced based on the shapes of widely encountered transient phenomena in the eddy currents on the surface of a steel mill in [14]. These new wavelets are high frequency oscillations enveloped by single and double-sided exponentials, a cosine-tapered rectangle, and Gaussian, Hanning and Hamming functions. A time-frequency scale distribution was developed and its power distribution was mapped onto a three dimensional image. Through analysis of these image patterns, detection and classification of faults is possible. Since the wavelets match specific transients, the modified wavelet transform can have a high sensitivity for certain applications.

In [15], a wavelet-based approach to detect increased load torque using a PI-type Closed-loop Torque Observer (PICTO) is developed. While most fault detection schemes are based on the current which allows for estimation of the electomagnetic torque, the PICTO provides an estimation of the mechanical torque instead by taking into account the model of the machine and the mechanical friction and inertia.

The DWT using the Haar wavelet is performed on the PICTO output and analysis is based on the wavelet and scaling coefficients at the first scale. The authors define the fault index, FI, in (1.4),

$$FI = \sqrt{\sum_{k \in z} \left(a_{j,k}^2 + d_{j,k}^2 \right)}$$
 (1.4)

where $a_{j,k}$ and $d_{j,k}$ are the scaling and wavelet coefficients of the DWT respectively. A fault is considered to exist if FI exceeds a predetermined threshold for at least 2 seconds. The frequency range for the faults targeted in this work is 0-25Hz. The techniques in this work are developed analytically using a simplified model of the system.

Although this system can provide an diagnostic for increased load torque, it can be be considered to be overly complex. The amplitude of the current could likely substitute for FI in (1.4).

In [16], tool fracture in drilling operations, which is the chipping, breakage, or severe deformation of the cutting edges of a drill bit, is analyzed. When tool fracture occurs, a larger motor torque is generated due to the tool acting on the broken cutting edges.

The authors show that tool fracture can be observed through the estimated motor torque. The torque is approximated as the square of one of the lowpass filtered, rectified, phase currents. The cutoff frequency of the lowpass filter is 166Hz. Increased amplitude of the estimated torque can indicate the presence of a tool fracture.

In [17–19], various diagnostic techniques are used to detect inner and outer race faults in bearings. It is of interest to determine the signatures in the spectrum of the vibration due to the bearing defects. In these papers, the expected frequencies associated with the occurrence of the faults are lower than 250Hz. It can be observed in the spectrum, however, that excitation not only occurs at the expected frequencies, but also at higher frequencies, up to 12kHz. The expected frequencies are based on the frequency of occurrence of the faults, i.e. the inverse of the period which successive balls contact one point in the race. The higher frequencies are due to the event that occurs each time a ball contacts the damaged part of the race. In the present research, fault identification is based on the higher frequencies due to the individual events.

In [20–22], various diagnostic techniques are used to detect faults in gears. The faults pertain to a single tooth that is missing, cracked, or has a notch cut in it. Of particular interest are the signatures in the spectrum of the vibration due to the gear defects. In these papers, the toothmeshing frequency, i.e. the frequency which the defective tooth makes contact, ranges from 250 - 500Hz. This can be considered

to be the frequency of occurrence of the fault. It can be observed, however, that significant excitation occurs not only at the toothmeshing frequency, but at higher frequencies as well, up to approximately 5kHz. The higher frequencies are due to the event that occurs each time the defective tooth makes contact. Fault identification methods based on the higher frequencies due to the individual events are developed in the present research and are discussed in Section 4.1.

1.1.3 Methods to Detect Both Electrical and Mechanical Faults

The techniques presented in [23–26] were developed to detect the presence of several faults in automotive permanent magnet brush DC machines, mostly attributed to improper assembly. Both windshield wiper motors and fuel pump motors were used. The input coefficients to three fault detection algorithms were the modulus maxima of the first ten scales of the wavelet transform of the DC current.

The first algorithm applied a decision tree to the input coefficients. The decision tree indicated whether a fault was detected as well as its classification.

The second algorithm represented a refinement of the first and included a training phase. During the training phase, coefficients from motors with known faults were normalized and averaged. The resultant coefficients served as the centers of different fault clusters. Machines suspected of having faults, determined through a detection algorithm, were subject to a classification algorithm which used the nearest neighbor rule to determine the nearest fault cluster.

The third algorithm expanded on the classification algorithm used in the second algorithm by employing linear discriminant functions. This allowed the shape of the fault clusters to be tuned through the addition of a new set of weighting coefficients.

The faults in the windshield wiper motors included excess sealant applied during assembly causing one of the brush springs to become stuck, a kinked brush spring, a

gear tooth removed from a gear reduction mechanism, shaft misalignment caused by the failure to install a bushing during assembly, increased friction caused by insufficient grease being applied during assembly, and a faulty parking mechanism. The faults in the fuel pump motors included increased resistance in one coil, and scoring of the commutator face during assembly.

The system can operate under any load conditions and without knowledge of machine parameters. The system should be effective for other motor designs, although it was only tested with brush DC motors. This system was implemented offline, although online implementation could be easily realized.

Several related techniques have been presented in [27–29] in which three-phase induction machines are analyzed. In [27], a single phase of stator current is monitored. The stator current spectrum is analyzed for the presence of harmonics indicating the possibility of two types of faults. In the case of air gap eccentricities, harmonics with frequencies predicted by (1.5)

$$f_{ecc} = f_e \left[1 \pm k \left(\frac{1-s}{\frac{p}{2}} \right) \right] \tag{1.5}$$

are observed, where f_e is the electrical supply frequency, k = 1, 2, 3, ..., s is the per unit slip, and p is the number of machine poles. In the case of rolling-element bearing defects, harmonics with frequencies predicted by (1.6)

$$f_{bng} = |f_e \pm m \cdot f_v| \tag{1.6}$$

are observed where m = 1, 2, 3, ... and f_v is one of the characteristic vibration frequencies. While this technique is performed offline, it is expanded upon in [28] to be an online diagnostic. Additional frequencies are monitored to detect broken rotor

bars (1.7)
$$f_{brb} = f_e \left[k \left(\frac{1-s}{\frac{p}{2}} \right) \pm s \right]$$
 (1.7)

where due to the normal winding configuration, $\frac{2k}{p} = 1, 5, 7, 11, 13, \ldots$ A selective frequency filter is added along with an ANN. The selective frequency filter provides the ability to discern between frequency bands possibly related to specific faults. The filter has a learning stage where an adaptive threshold is calculated from the FFT components. The frequency components which exceed the calculated threshold are placed in a table. It also has a reducing stage where it is decided which table entries will be provided as inputs to the ANN. The ANN has a training phase where is forms clusters which represent valid motor operating conditions. As the ANN is exposed to more and varied operating conditions, the number of acceptable classifications increases. After the training phase, the ANN switches to a fault-sensing mode. When a spectral signature falls outside the trained clusters, it is tagged as a potential motor fault. The ANN alarms the user only after multiple indications of a potential fault have occurred protecting the ANN from alarming on random signals which have been incorrectly identified. The techniques presented in [27,28] do not require information on the motor or load characteristics.

In [29], the authors combine the techniques applied in [27,28], and expand upon them. In this case, all three stator currents as well as all line-line stator voltages are measured. A model-based thermal failure protection algorithm is added. This system was implemented online. It is claimed that the system can operate with any motor design and load condition with only nameplate motor data.

1.1.4 Methods to Detect Arcing Faults

An algorithm to detect arcing based on wavelet analysis is discussed in [30]. Four mother wavelets are considered for analysis (db4, sym5, bior3.1, coif4). The final

selection for which mother wavelet to use was based on the magnitude of the level 1 decomposition near the fault, and the ability to distinguish between the faulted and the healthy case.

The algorithm is based on the Maximum Sum Value of the DWT (1.8),

$$SUM_{-}d1 = \sum_{k=1}^{n} |d1(k)|$$
 (1.8)

where n is the length of the analysis window and d1 is the level 1 DWT. The following parameters are defined in the algorithm, the signal of interest being the Maximum Sum Value described above:

- 1. FC = Signal magnitude threshold to detect HIF (High Impedance Fault)
- 2. FI = Number of sequential samples for which SUM_d1 > FC
- 3. D = Number of samples for which a transient event, e.g. HIF, must persist continuously. This helps differentiate between HIF and nonfault transient events, e.g. capacitor and line switching, arc furnace loads, etc...

When FI=D, a HIF fault was said to be present. The sampling rate used was 3840 Hz (64 samples / cycle @ 60Hz). In this work, FC=0.085 and D=128 (2 cycles @ 60Hz). Capacitor and line switching and arc furnace loads momentarily exceed the threshold, FC, but for shorter duration (≤ 64 samples).

In [31], an arcing detection algorithm is developed based on the outputs of four sets of redundant sensors: Ultrasonic, infrared, radio frequency, and acoustic. When one of each type of sensor simultaneously exceeds its predetermined threshold, an arcing fault is said to exist. 100 samples of both pre- and post-fault data are stored and an image is captured with a video camera which helps to pinpoint the location of the arc.

1.1.5 Methods to Mitigate Faults

In [32], various control methods which can still provide output are explained for the following faults: Switch short or open circuits; phase-leg short circuits; and single-phase open circuits. The various drive topologies and control strategies are rated using the Fault Power Rating Factor (FPRF) and the Silicon Overrating Cost Factor (SOCF) defined in (1.9–1.10).

$$FPRF = \frac{\text{maximum kVA output during fault}}{\text{max. kVA output of std. unfaulted inverter}}$$
(1.9)

$$SOCF = \frac{\text{weighted kVA rating of all switches}}{\text{kVA rating of standard inverter switches}}$$
 (1.10)

Switches are weighted by the rules in (1.11–1.12).

$$1 SCR = 0.5 IGBT \tag{1.11}$$

$$1 \text{ TRIAC} = 1 \text{ IGBT} \tag{1.12}$$

The baseline in this work is a standard inverter using SVPWM w/o overmodulation where the peak phase voltage is 0.577pu and the peak phase current is 1pu (switches are rated for 1pu voltage and 1pu current). In a standard three-phase inverter, having no starting capacity as well as large torque ripples in the event of a fault, FPRF=0 and SOCF=1. In this work, 9 topologies are explained and rated using FPRF and SOCF. A description, the FPRF, and the SOCF for each topology are outlined in Table 1 in [32], shown in Fig. 1.4.

Work on an open-loop V/F drive was performed in [33]. The faults of interest were the presence of an open gate drive and a device short circuit. In the case of a device short circuit, an additional switch is required to isolate the faulty leg. Typically, when running in single-phase mode, there is a large second harmonic pulsating torque.

			ſ	I rating of		Silison	Fault tolerant to							
Topology	Fuses	Split DC bus?	Auxiliary Switches	auxiliary switches (per unit)	Fault Power Rating Factor (FPRF)	Overrating Cost Factor (SOCF)	1 switch short	Phase-leg short	1 switch open	1 phase open				
Standard (Fig. 1)	0	N	None	N/A	0	1	1	Not fault	tolerar	nt				
Switch-redt. Top. (Fig. 5) for open- phase faults	0	Υ	1 (TRIAC)	1.73	0.50	1.29				X				
Switch-redt. Top. (Fig. 5) for shorted switch faults	3	Υ	3 (TRIAC)	1.00	0.50	1.50	х		X					
Switch-redundant topology (Fig. 5)	3	Y	3 (TRIAC) 1 (TRIAC)	1.00 1.73	0.50	1.79	х		X	х				
Double switch-redundant topology with a four terminal motor (Fig. 9)	8	N	8 (SCR) 2 (IGBT)	1.00 (SCR) 1.73 (IGBT)	0.58	2.24	x	x	х	x				
Phase-redundant topology with a three terminal motor (Fig. 10)	6	N	6 (SCR) 3 (TRIAC) 2 (IGBT)	1.00 (SCR) 1.00 (TRIAC) 1.00 (IGBT)	1.0	2.33	x	x	x	x				
Cascaded inverter topology (Fig. 11)	0	N	None	N/A	0.58	1.15				х				
Cascaded inverter topology w/ TRIACs (Fig. 11)	0	N	3 (TRIAC)	1.00	0.58	1.44	X		х	х				
Four-leg inv. top. w/ 2-phase control (Fig. 12)	0	N	2 (IGBT)	1.73	0.58	1.58				х				
Four-leg inv. top. w/ unipolar control (Fig. 12)	0	N	2 (IGBT)	1.73	0.58	1.58			х					

Figure 1.4. Characteristic Ratings of Fault Tolerant Inverter Topologies

Upon detection of these faults, lower order harmonic torques can be neutralized by injecting odd harmonic voltages at the appropriate phase angles.

CHAPTER 2

Theory

2.1 Fast Fourier Transform

The Fourier Transform gives the spectrum of a signal. It is best suited for the analysis of stationary signals, or signals whose spectrum remains constant. The FFT is used to determine the spectrum of discrete-time signals. Tiling in the time-frequency plane for the FFT in Fig. 2.1 shows that the spectrum of the signal is divided into several frequency bands, however no information is present on the time axis. The faults studied in this work, on the other hand, manifest themselves as short transients superimposed on the stator currents. Analysis of these short transients requires information

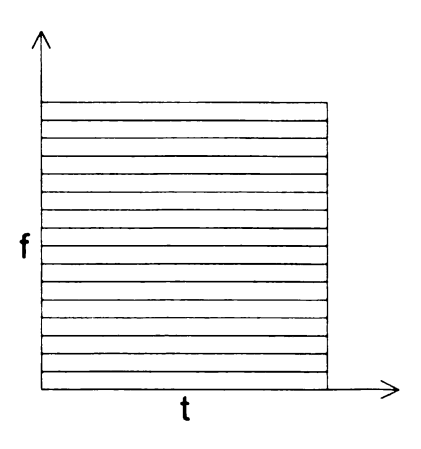


Figure 2.1. FFT Tiling

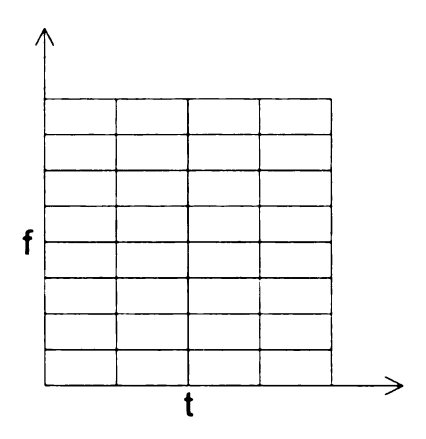


Figure 2.2. STFT Tiling

in both frequency and time. The inability to provide time localization of a signal is a fundamental limitation of the FFT.

2.2 Short-Time Fourier Transform

The STFT [34] is an extension of the FFT, allowing for the analysis of non-stationary signals. Here, the signal is broken up into small time sections, and each is analyzed using the FFT. The results for of the STFT are intuitive and easy to correlate with the original signal. Tiling for the STFT in Fig. 2.2 shows how the spectrum of a signal changes with time. The tiling for the STFT is uniform in both time and frequency. In the implementation of the STFT, a design tradeoff must be made between time and frequency resolution. This is due to the uncertainty principle, which limits the lower bound on the time-bandwidth product (2.1).

$$TB \ge \frac{1}{2} \tag{2.1}$$

A block diagram for the STFT algorithm is shown in Fig. 2.3, where *nfft* is the length of the DFT, *noverlap* is the number of samples the two frames overlap, and

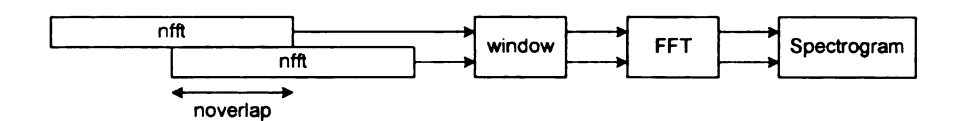


Figure 2.3. STFT Block Diagram

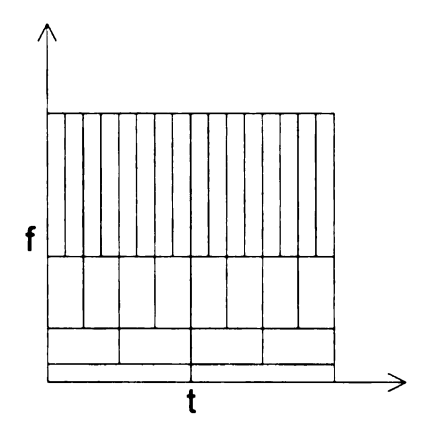


Figure 2.4. DWT Tiling

window is a weighting vector applied to the FFT input. The spectrogram is a plot of the magnitude square of the STFT. It is similar to the tiling shown in Fig. 2.2, with color shading denoting the energy in each tile.

2.3 Discrete Wavelet Transform

Wavelet analysis [35] is also suitable for non-stationary signals. The DWT has greater flexibility than the STFT. Different basis functions, or mother wavelets, may be used in wavelet analysis while the basis function for Fourier analysis is always the sinusoid. Unlike sinusoids, wavelets have finite energy concentrated around a point. One can choose, or design a wavelet to achieve the best results for a specific application.

Tiling for the DWT is shown in Fig. 2.4. Unlike Fourier methods, the tiling for the DWT is variable allowing for both good time resolution of high frequency

components, and good frequency resolution of low frequency components in the same analysis.

The Hilbert space of measurable, square-integrable functions, $f(x) \in L^2(\mathbf{R})$, is defined in (2.2).

$$\int_{-\infty}^{+\infty} |f(x)|^2 dx < +\infty \tag{2.2}$$

A basis for a space \mathcal{V} is defined as a set of linearly independent functions that span the space. That is, any function in \mathcal{V} can be written as a linear combination of the basis functions. This can be illustrated by a linear decomposition (2.3), where f(t) represents any function in the space \mathcal{V} , $\psi_{\ell}(t)$ are the basis functions, and a_{ℓ} are the scaling coefficients.

$$f(t) = \sum_{\ell} a_{\ell} \psi_{\ell}(t) \tag{2.3}$$

The discrete wavelet transform can be defined using the idea of multiresolution by starting with the scaling function and defining the wavelet function in terms of it. A basic one-dimensional scaling function can be designed to translate a function in time (2.4) where **Z** is the set of all integers.

$$\varphi_k(t) = \varphi(t - k) \quad k \in \mathbf{Z} \quad \varphi \in L^2$$
 (2.4)

Wavelet systems are two-dimensional, so a scaling function $\varphi_{j,k}(t)$ that both scales and translates a function $\varphi(t)$ is defined in (2.5),

$$\varphi_{j,k}(t) = 2^{j/2} \varphi \left(2^j \left(t - 2^{-j} k \right) \right) \quad j, k \in \mathbf{Z} \quad \varphi \in L^2, \tag{2.5}$$

where j is the \log_2 of the scale and $2^{-j}k$ represents the translation in time. A subspace of the $L^2(\mathbf{R})$ functions can be defined as the scaling function space \mathcal{V} . $\varphi_{j,k}(t)$ spans the space \mathcal{V}_j , meaning that any function in \mathcal{V}_j can be represented by a linear combination of functions of the form $\varphi_{j,k}(t)$.

When discussing scaling functions in terms of multiresolution analysis the relationship between the span of scaling functions with different indices can be seen in (2.6-2.7).

$$\cdots \subset \mathcal{V}_{-2} \subset \mathcal{V}_{-1} \subset \mathcal{V}_0 \subset \mathcal{V}_1 \subset \mathcal{V}_2 \subset \cdots \subset L^2 \tag{2.6}$$

$$\mathcal{V}_{-\infty} = \{0\}, \quad \mathcal{V}_{\infty} = L^2 \tag{2.7}$$

Through this scaling, if a function $f(t) \in \mathcal{V}_j$, then $f(2t) \in \mathcal{V}_{j+1}$. In the case of the scaling function, $\varphi(t)$ is written as a function of $\varphi(2t)$ in (2.8),

$$\varphi(t) = \sum_{n} h_0(n) \sqrt{2} \varphi(2t - n), \quad n \in \mathbf{Z}$$
(2.8)

where h_0 is a set of coefficients discussed in Section 2.4.

Another subspace of the $L^2(\mathbf{R})$ functions is the wavelet vector space \mathcal{W} . A wavelet spans the space \mathcal{W}_j , which represents the difference between two scaling function spaces, \mathcal{V}_j and \mathcal{V}_{j+1} . It can be seen that (2.9) extends to (2.10).

$$\mathcal{V}_1 = \mathcal{V}_0 \oplus \mathcal{W}_0 \tag{2.9}$$

$$L^2 = \mathcal{V}_0 \oplus \mathcal{W}_0 \oplus \mathcal{W}_1 \oplus \cdots \tag{2.10}$$

The relationship between the scaling function and wavelet vector spaces is illustrated in Figure 2.5.

The scale of the initial space V_j can be chosen arbitrarily, but is usually chosen to be the coarsest detail of interest in a signal. It can even be chosen as $j = -\infty$ where L^2 can be reconstructed in terms of only wavelet functions (2.11).

$$L^{2} = \cdots \oplus \mathcal{W}_{-2} \oplus \mathcal{W}_{-1} \oplus \mathcal{W}_{0} \oplus \mathcal{W}_{1} \oplus \mathcal{W}_{2} \oplus \cdots$$
 (2.11)

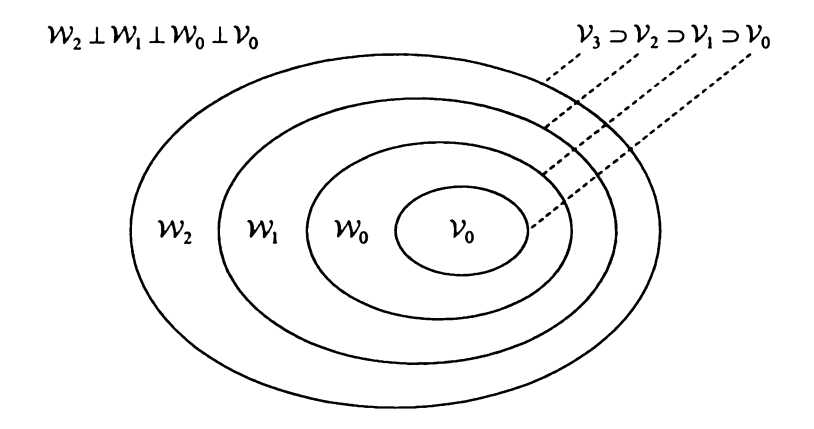


Figure 2.5. Scaling Function and Wavelet Vector Spaces

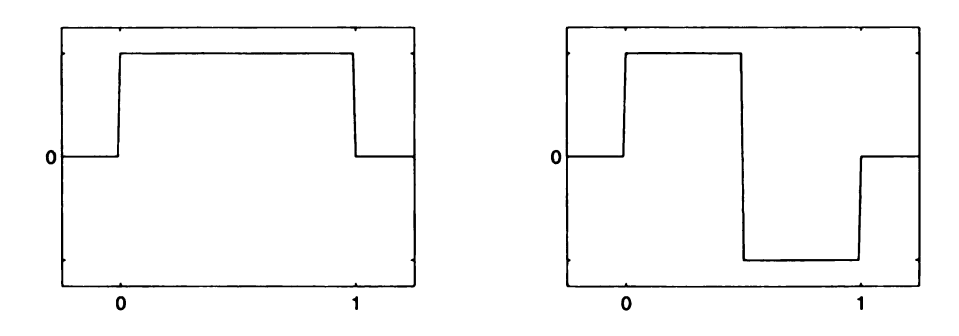


Figure 2.6. Haar Scaling and Wavelet Functions

In the case of the wavelet function, $\psi(t)$ is written as a function of $\varphi(2t)$ in (2.12),

$$\psi(t) = \sum_{n} h_1(n)\sqrt{2}\varphi(2t - n), \quad n \in \mathbf{Z}$$
 (2.12)

where h_1 is a set of coefficients discussed in Section 2.4.

A very basic wavelet system with a scaling function and a wavelet function to make up the detail between one level of decomposition and the next is the Haar system shown in Figure 2.6.

Any function in $L^2(\mathbf{R})$ can be written as an expansion of a scaling function and wavelets (2.13), where $c_{j_0}(k)$ are the scaling function coefficients, $\varphi_{j_0,k}(t)$ is the scaling

function at the initial scale j_0 , $d_j(k)$ are the wavelet function coefficients and $\psi_{j,k}(t)$ are the wavelet functions spanning the space between \mathcal{V}_{j_0} and L^2 .

$$f(t) = \sum_{k=-\infty}^{\infty} c_{j_0}(k)\varphi_{j_0,k}(t) + \sum_{k=-\infty}^{\infty} \sum_{j=j_0}^{\infty} d_j(k)\psi_{j,k}(t)$$
 (2.13)

2.4 Filter Banks

In order to perform the Discrete Wavelet Transform on a computer, computational methods must be developed. The DWT can be performed without using calculus, but rather additions and multiplications in the form of convolutions [35].

If we consider the linear decomposition in (2.3), and if the basis functions are orthogonal (2.14),

$$\langle \psi_k(t), \psi_\ell(t) \rangle = \int \psi_k(t) \psi_\ell(t) dt = 0, \quad k \neq \ell$$
 (2.14)

the coefficients of the decomposition, a_k , can be determined by calculating the inner product (2.15).

$$a_k = \langle f(t), \psi_k(t) \rangle = \int f(t)\psi_k(t)dt$$
 (2.15)

In the two-dimensional case of the wavelet transform, the same techniques can be used to calculate the scaling coefficients (2.16) and the wavelet coefficients (2.17).

$$c_{j}(k) = \langle f(t), \varphi_{j,k}(t) \rangle = \int f(t)\varphi_{j,k}(t)dt$$
 (2.16)

$$d_j(k) = \langle f(t), \psi_{j,k}(t) \rangle = \int f(t)\psi_{j,k}(t)dt$$
 (2.17)

Finally the scaling function coefficients for a coarse scale can be determined from the scaling function coefficients at the next finer scale by convolving the coefficients

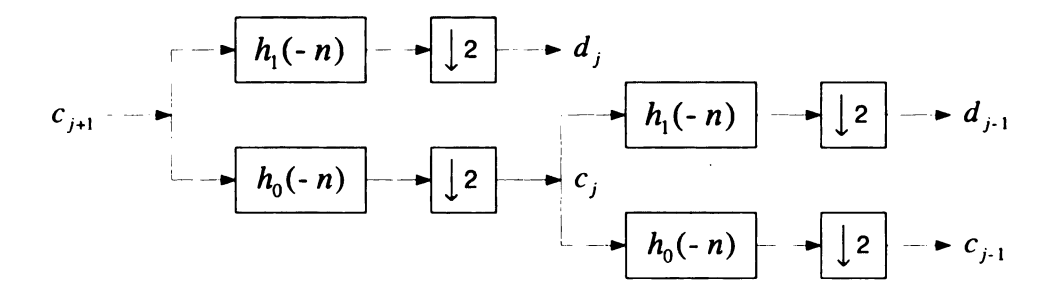


Figure 2.7. Two-Stage Filter Bank Analysis Tree

at the finer scale with the recursion coefficients $h_0(n)$ and then down-sampling (2.18).

$$c_j(k) = \sum_{m} h_0(m - 2k)c_{j+1}(m)$$
 (2.18)

The coefficients $h_0(n)$ are referred to as the decomposition lowpass filter coefficients. The same can be done in the case of the wavelet coefficients using the recursion coefficients $h_1(n)$ (2.19) where $h_1(n) = (-1)^n h_0(1-n)$.

$$d_j(k) = \sum_{m} h_1(m-2k)c_{j+1}(m)$$
 (2.19)

The coefficients $h_1(n)$ are referred to as the decomposition highpass filter coefficients. An example of a filter bank analysis tree is illustrated in Figure 2.7.

The down-sampling operation does not result in the loss of signal information. In the filter bank structure shown in Figure 2.7, there is enough information to reconstruct c_{j+1} in either the combination of c_j and d_j , or the combination of c_{j-1} , d_{j-1} and d_j . Despite down-sampling, either of these combinations of coefficients will have approximately the same number of values as c_{j+1} . Signal reconstruction from DWT coefficients is not used in this work, however it is discussed in detail in [35].

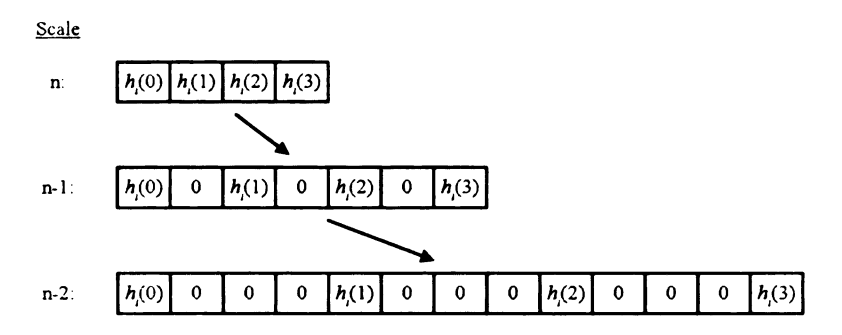


Figure 2.8. UDWT Filters Modified by the "Algorithme à Trous"

2.5 Undecimated Discrete Wavelet Transform

One of the drawbacks of the DWT is that it is not a shift-invariant transformation. This makes pattern recognition problems based on the DWT more difficult since the DWT coefficients resulting from decomposition of a signal and a shifted version of the signal can be very different. Only in special cases, where the signal is shifted by specific powers of two will the outputs be shifted versions of one another.

The UDWT adds the property of shift-invariance to the DWT. Here, the down-sampling step is omitted from the DWT algorithm, and zeros are inserted between the filter coefficients at each successive scale, as shown in Fig. 2.8. This is known as the "Algorithme à Trous" [36, 37]. While circular convolution is used in [36], linear convolution is used here, since the signals are not periodic. The coefficients at each end of the convolution where the filter and the signal are not completely overlapping, known as end effects, are replaced by zeros. As these zeros propagate through each scale of the UDWT, the number of end effect coefficients increases. The fact that the length of the wavelet filters increase at each scale also contributes to additional end effects.

An example to show the shift-invariant property of the UDWT is in Fig. 2.9. Here, the DWT and UDWT of a signal and the same signal shifted by six samples are compared. The first row shows the non-shifted and shifted signals. The second

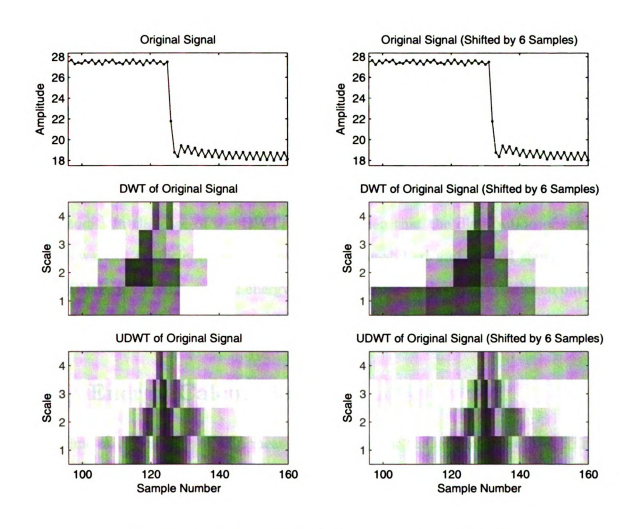


Figure 2.9. Example of Shift-Invariance of the UDWT

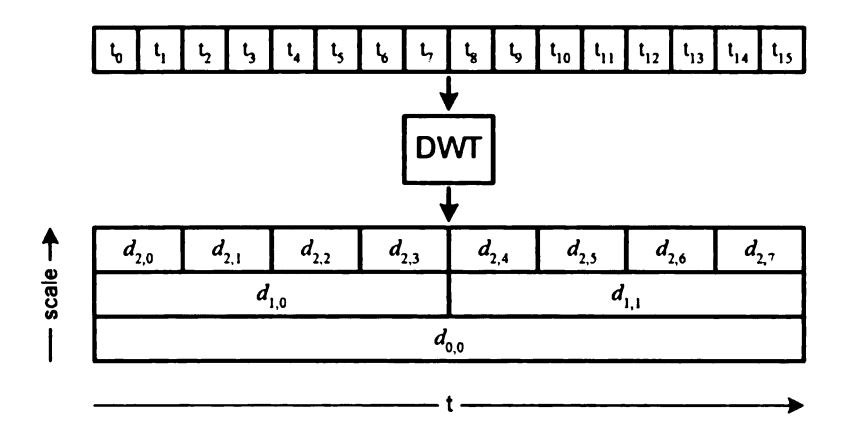


Figure 2.10. Example DWT Showing Coefficient Indices

and third rows show the DWT and UDWT of these signals. The value of the wavelet coefficients is denoted by shading, with the darkest coefficients having the highest amplitude. In the case of the DWT, it can be seen that the distribution of energy in the wavelet coefficients is different for the non-shifted and shifted signals. For the UDWT, the distribution of energy is consistent for both signals, with the output coefficients shifted by the same number of samples as the input signal.

2.6 Energy Calculations

The time-marginal is used as a measure of energy for the coefficients of the STFT.

This is defined as the sum of the squares of the coefficients at each time step.

In the case of the wavelet transform, three methods for determining the energy have been explored. Each weights the coefficients in various scales differently. An example of the coefficient indices for the following methods is shown in Fig. 2.10.

The first method gives equal weighting to coefficients in all scales, and is most similar to the time marginal used for the STFT. When used for the DWT, the fact that there are fewer coefficients at lower scales makes it difficult to determine exactly the time of inception and clearing of a fault. For example, the energy at t_2 based on

the coefficient indices in Fig. 2.10 is computed using (2.20).

$$E(t_2) = d_{2,1}^2 + d_{1,0}^2 + d_{0,0}^2 (2.20)$$

The second method computes the energy based only on the coefficients at the highest scale, or the scale at the highest frequency. This method proved to have problems distinguishing between edges of faults and other high frequency phenomena in the signal, e.g. noise. For example, the energy at t_2 based on the coefficient indices in Fig. 2.10 is computed using (2.21).

$$E(t_2) = d_{2,1}^2 (2.21)$$

The third method gives increasing weight to coefficients in higher scales. This gives more emphasis to the high frequency information in the signal, but does not discard low frequency information entirely. This weighting proved to have the best balance between the first two methods, giving better accuracy than the first, and more noise immunity than the second. For example, the energy at t_2 based on the coefficient indices in Fig. 2.10 is computed using (2.22).

$$E(t_2) = d_{2,1}^2 \cdot 2^2 + d_{1,0}^2 \cdot 2^1 + d_{0,0}^2 \cdot 2^0$$
 (2.22)

2.7 Categorization

In this work, the currents in the drive are analyzed using either Fourier or wavelet analysis. When the presence of a fault in the drive is detected, the analysis coefficients are categorized, with the possible categories corresponding to one of several known fault types.

To accomplish this categorization, a variety of techniques are available. At the

onset of this work, the nearest neighbor rule was used. Further refinement of the algorithms led to the use of linear discriminant analysis, which added a training procedure to improve the design of the classification algorithm. These techniques are discussed in detail in Sections 2.7.1-2.7.2.

In this work, the effect of the duration of the fault event was determined in three different ways. In the first case, the coefficients at each time sample were treated as independent and classified separately. In the second case, the coefficients corresponding to the entire duration of the fault event were classified together. Finally, in the third case, the coefficients corresponding only to either the inception or the clearing of a fault were classified separately from each other.

There are several other techniques which are commonly used for these types of problems, including thresholding, Artificial Neural Networks, and Support Vector Machines.

A novel method to recognize words in a bitmapped representation of a faxed document is developed in [38]. A transform developed by the authors, the Scale and Translation Invariant Representation (STIR), is used as a preprocessing step, prior to the classification algorithm. The STIR can be used when the object to be recognized has a consistent shape and appears on a constant intensity background.

To calculate the STIR, the authors first compute the 2-D discrete autocorrelation of the signal (2.23)

$$A(k_1, k_2) = \sum_{n_1, n_2} \sum_{n_2} a(n_1, n_2) a(n_1 - k_1, n_2 - k_2)$$
(2.23)

where $a(n_1, n_2)$ is the image. This removes translational effects of the signal.

Next, to remove scaling effects, the 2-D direct scale transform is applied to two discrete quadrant functions of the autocorrelation plane which are defined in (2.24)

and (2.25).

$$Q_1(k_1, k_2) = A(k_1, k_2)$$
 for $k_1, k_2 \ge 0$ (2.24)

$$Q_2(k_1, k_2) = A(k_1, -k_2)$$
 for $k_1, k_2 \le 0$ (2.25)

The continuous-time scale transform is defined in [39] as (2.26).

$$D(c) = \frac{1}{\sqrt{2\pi}} \int_0^\infty f(t) \frac{e^{-jc \ln t}}{\sqrt{t}} dt$$
 (2.26)

A discrete-time form of the 2-D direct scale transform was developed by the authors in [40] as (2.27).

$$D(c) \approx \left(\frac{1}{(1/2 - jc)\sqrt{2\pi}}\right) \sum_{k=1}^{\infty} \left[f(kT - T) - f(kT) \right] (kT)^{1/2 - jc}$$
 (2.27)

Normalization of the resultant scale transformed quadrant functions represents the STIR of the original 2-D input.

One downside to using autocorrelation to compute the STIR is the fact that the autocorrelation of the image is the same as that of a 180 degree rotated version of the image. In the case of word spotting, the authors found that it was difficult to classify between "b" and "p" and between "u" and "n". Some additional steps must be taken to account for this.

The authors present two approaches for classification. The first approach uses standard techniques. Here, training data is used to generate templates for each class. A similarity measure, such as correlation coefficient, between the processed test data and each template is calculated.

The second approach uses noise subspace methods. Here, an orthogonal subspace is created for each class of training data. A measure of the projection of the test data onto each of the subspaces is calculated. Test data matching a given class should be orthogonal to the noise subspace for that class and yield a small projection value.

2.7.1 Nearest Neighbor Rule

In order to categorize a sample point in d-dimensional space into a set of previously classified points, one technique is the nearest neighbor rule (1-NN). It is assumed that observations which are close to each other (in some appropriate metric) will have the same classification [41]. This problem can be approached in two different ways, first, by assuming that some statistical distribution is given for the data, and second, by assuming no knowledge of a distribution except for what can be concluded from the samples. In this work, the focus is on the second method, where no probabilistic model of a distribution is assumed.

In calculating the minimum distance, some appropriate measure needs to be used. Any dissimilarity measure (2.28) would be applicable, however the most commonly used dissimilarity measures are the Minkowski p metrics (2.29), where d is the dimensionality of the vectors \mathbf{X}_m and \mathbf{X}_n [42].

$$d(\mathbf{X}_m, \mathbf{X}_n) = g\left[\sum_{i=1}^d f_i(X_{im}, X_{in})\right]$$
(2.28)

$$d(\mathbf{X}_m, \mathbf{X}_n) = \left[\sum_{i=1}^d |X_{im} - X_{in}|^p\right]^{\frac{1}{p}} \quad (p \ge 1)$$
 (2.29)

The three most often used Minkowski metrics are the taxi-cab distance (2.30) where p=1, the Euclidean metric (2.31) for which p=2 and the maximum coordinate distance (2.32) where $p=\infty$.

$$d(\mathbf{X}_{m}, \mathbf{X}_{n}) = \sum_{i=1}^{d} |X_{im} - X_{in}|$$
 (2.30)

$$d(\mathbf{X}_m, \mathbf{X}_n) = \left[\sum_{i=1}^d (X_{im} - X_{in})^2 \right]^{\frac{1}{2}}$$
 (2.31)

$$d(\mathbf{X}_m, \mathbf{X}_n) = \max_{1 \le i \le d} \{ |X_{im} - X_{in}| \}$$
 (2.32)

2.7.2 Linear Discriminant Analysis

A second approach to categorizing points in a d-dimensional space relies on the use of discriminant functions. In the implementation of discriminant functions, no prior knowledge of a probability distribution among the sample points is assumed. The space is divided into K regions, each having its own weighting coefficients. In this work, linear discriminant functions (2.33) [43] are used,

$$D_k(\mathbf{x}) = x_1 \alpha_{1k} + x_2 \alpha_{2k} + \dots + x_N \alpha_{Nk} + \alpha_{N+1,k}$$

$$k = 1, 2, \dots, K$$
(2.33)

where x is the N-dimensional sample vector and α are the normalized weighting coefficients for the k-th class. Linear discriminant functions were chosen for the algorithm since they are the most computationally efficient form. A sample vector belongs to a particular class if its discriminant function is greater for that class than for any other class, i.e., \mathbf{x}_i belongs to class C_j if

$$D_j(\mathbf{x}) > D_k(\mathbf{x})$$
 for every $k \neq j$.

The weighting coefficients are adjusted from their initial guess through a training procedure using sample vectors which the proper classification is known. The algorithm for this procedure makes adjustments to the weighting coefficients until each sample vector is correctly classified.

Young and Calvert [43] show that this training algorithm will converge in a finite number of steps. When a sample vector is correctly classified, no adjustment to the weighting coefficients is made. When a sample vectors is incorrectly classified, or

$$D_i(\mathbf{x}) \leq D_l(\mathbf{x}),$$

where

$$D_l(\mathbf{x}) = \max_{l \neq j} [D_1(\mathbf{x}), \dots, D_K(\mathbf{x})],$$

adjustments are made to α_j (2.34) and α_l (2.35) only,

$$\alpha_j(i+1) = \alpha_j(i) + a\mathbf{x}_i \tag{2.34}$$

$$\alpha_l(i+1) = \alpha_l(i) - a\mathbf{x_i}, \tag{2.35}$$

where a is a gain constant.

2.8 Cross Validation

Nonparametric estimation of statistical error is discussed in [44]. Error refers to either the bias and standard error of an estimator, or the error rate of a data-based prediction rule. In this research, the latter form of error is of concern.

In order to develop a robust pattern recognition algorithm with a limited amount of data available, cross validation can be used. Cross validation is a method to evaluate a learning-based classifier. This is commonly used when not enough data is available to have both a complete training set and a testing set. Instead, training is done on a subset of the data, and testing is done on the remaining data. The procedure for cross validation follows:

- 1. Delete the points x_i from the data set one at a time
- 2. Recalculate the prediction rule on the basis of the remaining n-1 points
- 3. See how well the recalculated rule predicts the deleted point
- 4. Average these predictions over all n deletions of an x_i

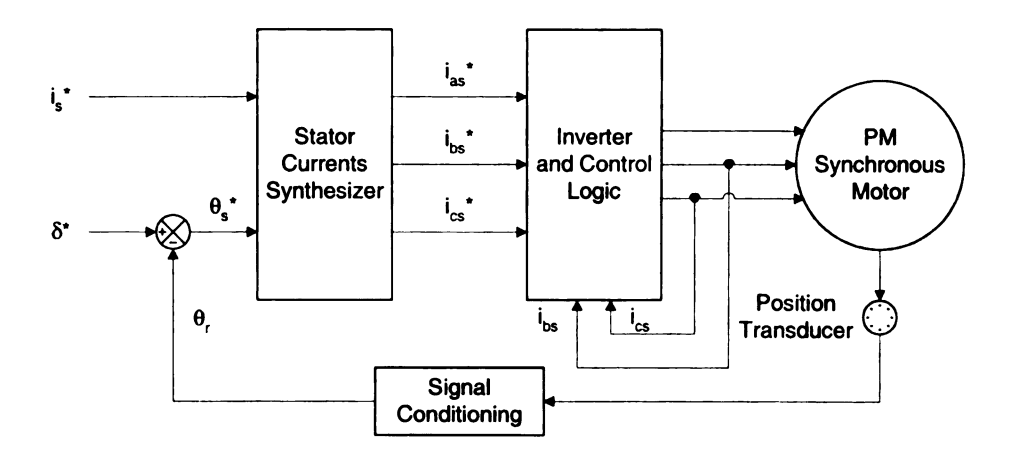


Figure 2.11. Vector-Controlled PMSM Drive

Good results from cross validation imply that the classes are separable. Additionally, newly acquired data are likely to be classified correctly.

2.9 PMSM Torque Control

A block diagram describing the implementation of vector control for a PMSM [45] is shown in Fig. 2.11, Where i_s^* is the stator current command phasor magnitude, δ^* is the torque angle command, θ_r is the rotor electrical angle, θ_s^* is the instantaneous position of the stator current phasor command, i_{as}^* , i_{bs}^* , and i_{cs}^* are the stator phase current commands, and i_{bs} and i_{cs} are measured stator phase currents.

The commands for i_s^* and δ^* are given by (2.36)-(2.37),

$$i_s^* = \sqrt{(i_{ds}^*)^2 + (i_{qs}^*)^2}$$
 (2.36)

$$\delta^* = \tan^{-1} \left[\frac{i_{qs}^*}{i_{ds}^*} \right] \tag{2.37}$$

where i_{qs}^* is the torque-producing component, and i_{ds}^* is the flux-producing component of the stator current command. Then, the stator phase current commands are defined

in (2.38)-(2.40).

$$i_{as}^* = i_s^* \sin\left(\theta_r + \delta^*\right) \tag{2.38}$$

$$i_{bs}^* = i_s^* \sin\left(\theta_r + \delta^* - \frac{2\pi}{3}\right) \tag{2.39}$$

$$i_{cs}^* = i_s^* \sin\left(\theta_r + \delta^* + \frac{2\pi}{3}\right) \tag{2.40}$$

Constant torque-angle control has been implemented where $\delta^* = \pi/2$. This mode of operation gives the maximum torque, and it suitable for operating speeds up to the base speed. In this case, the d-axis, or flux-producing component, of the stator current command is set at zero. Therefore, $i_s^* = |i_{qs}^*|$.

The stator phase currents i_{bs} and i_{cs} are measured during operation. The sum of the phase currents is defined as zero, so the remaining phase current is defined in (2.41).

$$i_{as} = -(i_{bs} + i_{cs}) (2.41)$$

Since the proposed methods for fault prognosis use i_{qs} and i_{ds} , they are computed in (2.42)-(2.43)

$$i_{qs} = \frac{2}{3} \left[i_{as} \cos \left(\theta_r\right) + i_{bs} \cos \left(\theta_r - \frac{2\pi}{3}\right) + i_{cs} \cos \left(\theta_r + \frac{2\pi}{3}\right) \right]$$
 (2.42)

$$i_{ds} = \frac{2}{3} \left[i_{as} \sin \left(\theta_r \right) + i_{bs} \sin \left(\theta_r - \frac{2\pi}{3} \right) + i_{cs} \sin \left(\theta_r + \frac{2\pi}{3} \right) \right]$$
 (2.43)

2.10 Discrete-Time PI Controller

The outputs of the PMSM controller in this project are currents as discussed in Section 2.9, however the inputs of the inverter are voltages. A PI controller will allow voltage commands to be generated from the errors in the currents. The block diagram for a continuous-time PI controller is shown in Fig. 2.12, where i^* is the input

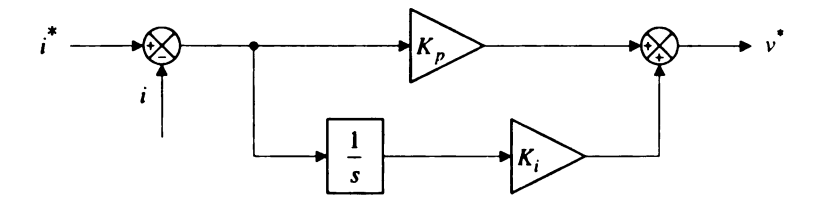


Figure 2.12. PI Controller

current command, i is the measured current, v^* is the output voltage command, K_p is the proportional gain, K_i is the integral gain, and 1/s is the transfer function for integration.

From Fig. 2.12, the transfer function in (2.44) can be determined.

$$\frac{v^*}{i^* - i} = K_p + \frac{K_i}{s} \tag{2.44}$$

To discretize the system, a discrete-time integrator, T/(z-1), using backward-rectangular integration replaces the continuous-time integrator, where T is the sample time.

The relationship between the output voltage command and input current command is described in (2.45).

$$\frac{v^*}{i^* - i} = K_p + \frac{T \cdot K_i}{z - 1}
v^* = K_p (i^* - i) + \frac{T \cdot K_i (i^* - i)}{z - 1}
v^* (z - 1) = K_p (i^* - i) (z - 1) + T \cdot K_i (i^* - i)
v^* z = v^* + K_p [(i^* - i) z - (i^* - i)] + T \cdot K_i (i^* - i)
v^*_{k+1} = v^*_k + K_p [(i^*_{k+1} - i_{k+1}) - (i^*_k - i_k)] + T \cdot K_i (i^*_k - i_k)
v^*_k = v^*_{k-1} + K_p [(i^*_k - i_k) - (i^*_{k-1} - i_{k-1})] + T \cdot K_i (i^*_{k-1} - i_{k-1})$$
(2.45)

CHAPTER 3

Applications

One application for this work is in the area of fault tolerant drives. Because of the small size, high power density and low audible noise of PMAC machines, they are strong candidates for use in X-by-wire and other fault tolerant systems in vehicles. Upon detection and classification of a drive fault, measures can be taken to mitigate the effect of the fault. This reduces the likelihood of failure of the drive.

Several fault tolerant drive configurations and corresponding mitigation techniques are discussed in [32,33,46]. The first [32] relies on additional hardware which is able to isolate short circuit faults. The techniques discussed can either isolate the fault and continue to operate in single-phase mode or isolate the fault and move the faulted phase to a different set of switches. The additional redundancy built into the drive adds cost.

A low-cost fault tolerant drive design allowing for continued operation of an induction motor in single-phase mode without adding any additional switches is developed in [33]. This type of system is typically able to run in the presence of open circuit faults, but its limitation is that it is not able to isolate short circuit faults.

Estimates of the reliability of permanent magnet AC drives are investigated in [46]. This was done for both healthy drives as well as faulted drives under remediation. The author identified the most critical components and faults in the drive, and explored

remedial mitigation techniques. Analysis was done to determine both device as well as overall system reliability. Examples of reduced operation and redundant hardware are included in the work.

The focus of the present work is the identification of intermittent drive faults. Upon identification, further measures, such as those discussed above, can be taken to mitigate the effect of the fault if it is determined to be advantageous.

The test machine used in this analysis is a six-pole surface mounted PMAC machine for an automotive application. The machine is operated in a vector drive with the torque angle set to $\pi/2$ [45]. This mode of operation minimizes losses in the machine, and is suitable for operating speeds up to the base speed. The torque-producing component of the stator current command was $i_{qs}^* = 0.3pu$, and the flux-weakening component $i_{ds}^* = 0$; the speed is controlled by the dynamometer and experiments were performed at both 10% and 15% the no-load speed.

Two different sets of values for the proportional and integral gains for the PI controllers, which generate voltage commands from the error in the current, were investigated. In the first set of experiments, referred to in Section 4.1 as 'Slow Controller Response', $K_p = 0.8$ and $K_i = 0.8$. In the second set of experiments, referred to as 'Fast Controller Response', $K_p = 0.55$ and $K_i = 1000$. The second set of experiments resulted in improved transient response and less steady state error compared to the first set of experiments.

The faults imposed in this work are not periodic. The time interval between successive faults is random, as well as the fault duration.

3.1 Electrical Drive Faults

In the literature, a variety of electrical PMAC drive faults have been explored, including increased contact resistance, turn-turn insulation failures, increased coil re-

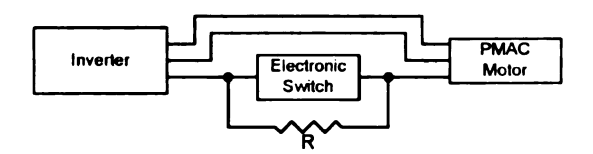


Figure 3.1. Experimental Mimic of Series Resistance Fault

sistance, voltage unbalances, inverter switch-on / switch-off failures, arcing, and DC supply failures. The present work focuses on increased contact resistance and turn-terminal shorts.

3.1.1 Intermittent Increased Contact Resistance

The first fault explored in this work is an intermittent increased contact resistance between the motor and the controller. An experiment was designed to simulate this. The fault is achieved by adding the parallel combination of a normally closed switch, and a resistance in series with one of the motor phases as shown in Fig. 3.1.

The fault is initiated by opening the switch for a short time interval, causing current to flow through the resistance. The switch is described in detail in Section 5.

Various values for the contact resistance were used, including 2.14pu, 2.80pu, 4.03pu, 6.33pu, and 15.84pu. The fault can be initiated at varying levels of the peak amplitude of the phase current command; 5%, 50%, and 95% were tried. Tests with fault durations of 5ms and 10ms have been performed to investigate invariance of the results with respect to this parameter as well.

3.1.2 Turn-Terminal Short

The second fault explored in this work is an insulation failure in the stator windings of the motor. The machine used in this experiment has multiple parallel stranded-wire windings per phase, each with several coils in series. To simulate this fault

in the experimental setup, at one point in a single strand of one of the windings, the insulation was removed, and a normally open switch was added between this point and the corresponding phase terminal of the motor. The fault was initiated by momentarily closing the switch, causing current to be split between the intended path and the switch. The interrupted windings and the windings with leads soldered to them are shown in Figs. 3.2(a) and 3.2(b) respectively.

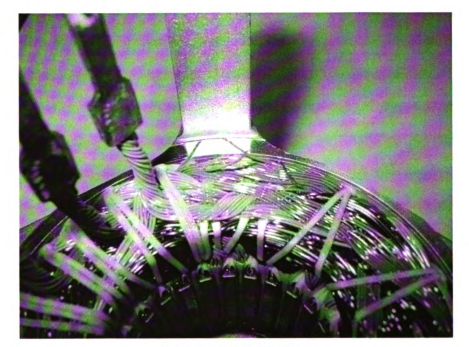
The fault can be initiated at varying levels of the peak amplitude of the phase current command; 5%, 50%, and 95% were tried. Additionally, tests with fault durations of 5ms and 10ms have been performed to investigate invariance of the results with respect to this parameter.

3.2 Mechanical Drive Faults

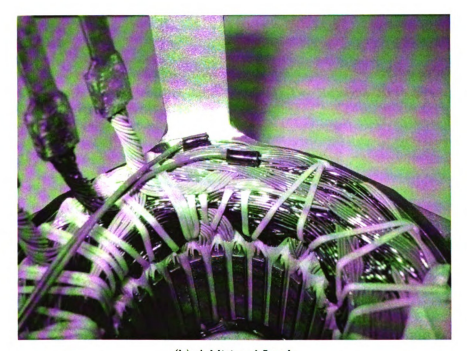
Techniques to detect a variety of mechanical PMAC drive faults have been developed by others, including damaged gear teeth, airgap eccentricities (static and dynamic), bearing defects, increased friction, and permanent magnet defects. The present work focuses on varying numbers of missing gear teeth.

3.2.1 Missing Gear Teeth

The third fault explored in this work is missing gear teeth in a gearbox coupled to the motor. The gearbox has two identical spur gears supported by a set of bearings. One of the gears is free of faults, and the following conditions of the mating gear have been tested: Healthy; one tooth missing; one tooth missing and its adjacent tooth severely worn; two adjacent teeth missing; and two adjacent teeth missing with their adjacent tooth severely worn. The gears are shown in Figs. 3.3(a)-3.3(e) respectively. Tests have been performed to recognize the fault and determine the number of missing teeth.



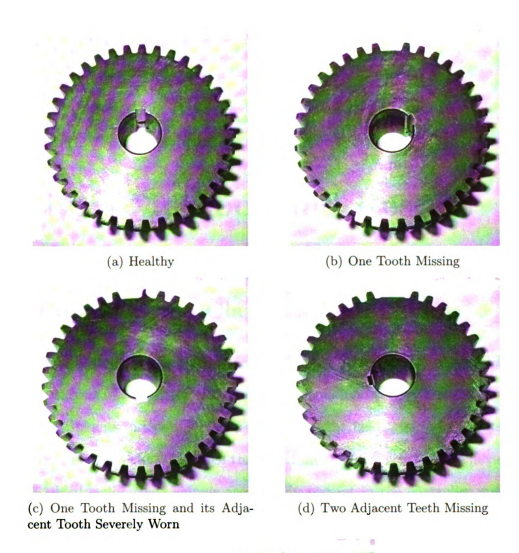
(a) Interrupted Windings



(b) Additional Leads

Figure 3.2. Turn-Terminal Short Stator Modifications

43





(e) Two Adjacent Teeth Missing and their Adjacent Tooth Severely Worn

Figure 3.3. Test Gears

CHAPTER 4

Analysis Methods and Results

4.1 Detection and Classification Methods

In this work, the detection and classification of faults described in Sections 3.1–3.2 are based on analysis of the stator currents of the machine. Rather than analyzing the three stator currents independently of each other, the field oriented currents i_{qs} and i_{ds} are used. This has the advantage that the fundamental electrical frequency is not present. Additionally, these signals are already present in the controller and require no additional hardware or computation. Consequently, rotor speed has little effect on the spectrum of these currents, allowing for invariance in the algorithm to rotor speed. Together, i_{qs} and i_{ds} are a complete representation of the stator currents, however, it has been determined experimentally that through analysis of i_{qs} only, accurate fault detection and classification can be achieved.

4.1.1 Algorithm Based on the FFT Applied to Electrical Faults (Slow Controller Response)

The algorithm developed in [47] is considered a precursor to the algorithms outlined in the upcoming sections. The input to the algorithm is the STFT of the measured q-axis current, i_{qs} . For this analysis, nfft=64, noverlap=48, and a 64-point rectan-

gular window is used. The parameters of the STFT are described in Section 2.2. The resultant STFT has 33 frequency bands, however the two outermost bands are discarded. The energy in these bands is far greater than in the inner bands of interest. The DC component of i_{qs} is approximately 30A, and the 10kHz component corresponds to the switching frequency. With the controller running at 20kHz, one switching event occurs at each time step. Two switching events correspond to one on/off period causing the increased energy at 10kHz. The algorithm is based on the remaining 31 frequency bands.

The algorithm has two parts; a detection phase and a classification phase. The detection phase of the algorithm is based on thresholding on the time marginal of the STFT. In this work, data from eight experiments on a healthy machine were analyzed, each containing 8,192 time samples resulting in 509 STFT samples. The threshold on the time marginal was set to be 25% greater than the largest which was observed in all 4,072 STFT samples from the healthy machine data. If the energy in new test data exceeds this threshold, a fault is considered to exist.

The classification phase was based on linear discriminant analysis. This phase is implemented when the criterion for detection is met. The data used to train the algorithm for the increased contact resistance fault, thereby determining the weighting coefficients, were 127 STFT samples from 16 experiments corresponding to both faults with 5ms and 10ms switch durations. The data used were the samples in the STFT corresponding to the inception and the clearing of the fault, but not the duration of time while the fault was present. The current quickly reached a new steady state operating point immediately after the switching event.

The data used to train the algorithm for the turn-terminal short were 199 STFT samples from 16 experiments corresponding to both 5ms and 10ms switch durations. The data used were the samples in the STFT corresponding to the beginning of the first switching event until the end of the second switching event.

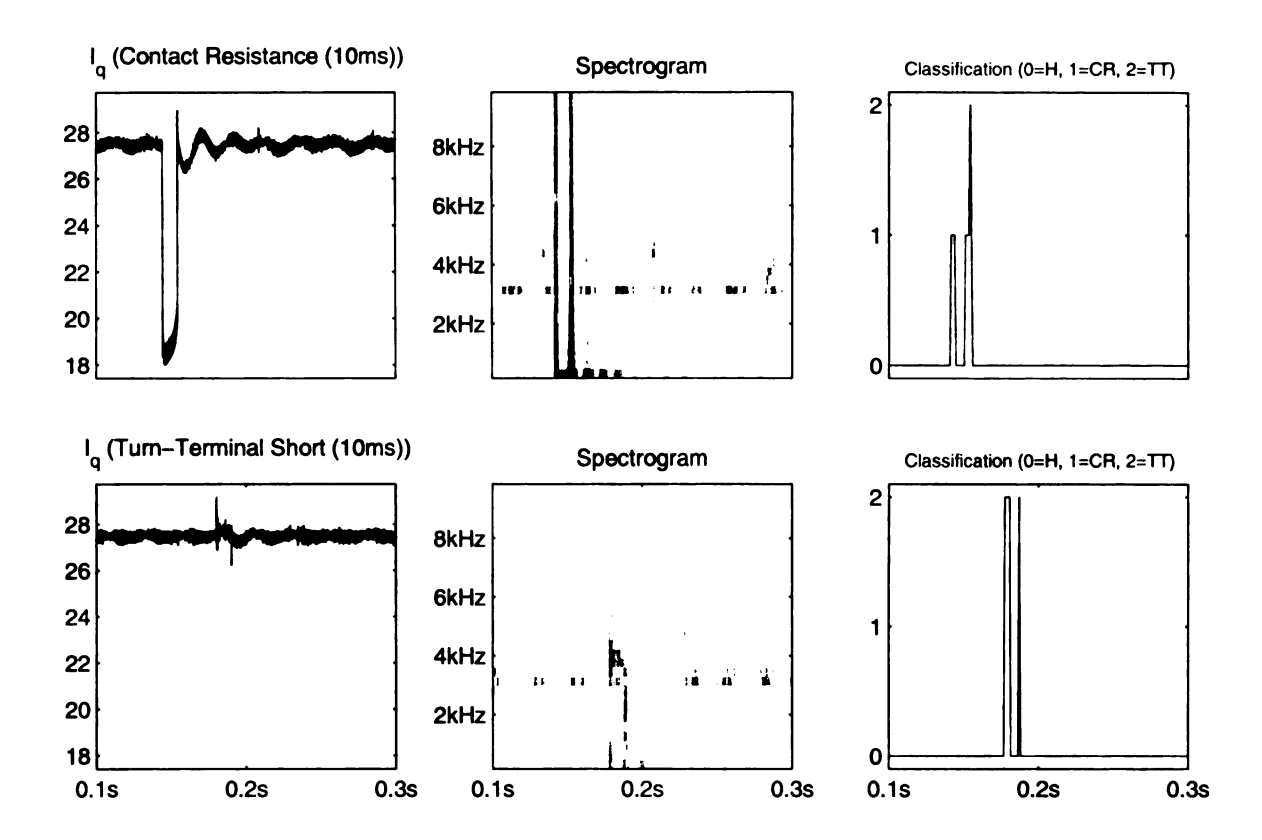


Figure 4.1. Typical Results (Section 4.1.1)

Following the training of the weighting coefficients, data that had not been used in the training algorithm were tested. One data set, each containing 8,192 time samples resulting in 509 STFT samples, from each of the following operating conditions was tested: Healthy; 5ms increased contact resistance; 10ms increased contact resistance; 5ms turn-terminal short; and 10ms turn-terminal short.

The results from two typical test cases are shown in Fig. 4.1. Here, only 250 of the 509 STFT points are displayed for improved clarity. The top row of Fig. 4.1 has results from the increased contact resistance fault. The bottom row has results from the turn-terminal short. The left column shows the measured torque producing component of the current, i_{qs} , for each test case. The center column shows the spectrogram of the data to the left. The right column is the output of the detection and classification algorithm with 0=healthy, 1=increased contact resistance fault, and

2=turn-terminal short.

In the first case, healthy, the detection criterion was not met, as intended. In the second case, increased contact resistance, the detection criterion was met during the switching events only as intended, and each sample was classified correctly with the exception of one. In the third case, turn-terminal short, the detection criterion was met for the switching events only, and each sample was classified correctly. In this case, although the weighting coefficients have been trained using samples corresponding to the beginning of the first switching event until the end of the second switching event, the criterion for detection was only met during the inception and the clearing of the fault.

4.1.2 Algorithm Based on the STFT Applied to Electrical Faults (Slow Controller Response)

The input to the algorithm developed in this section is 25 STFT samples, or 20ms, of the measured q-axis current, i_{qs} . This time interval is selected to capture the beginning and end of each fault separately. The algorithm has two parts; a detection phase and a classification phase. The detection phase of the algorithm is based on thresholding on the time marginal of the STFT. The threshold was set at 25% greater than the largest which was observed in all samples from the healthy machine data. If the energy in new test data exceeds this threshold, a fault is considered to exist.

The classification phase was based on linear discriminant analysis. This phase is implemented when the criterion for detection is met. To train the algorithm, thereby determining the weighting coefficients, data were used from eight experiments from each of the following operating conditions: Healthy, increased contact resistance (5ms and 10ms), and turn-terminal short (5ms and 10ms). The data used were the 25 samples in the STFT corresponding to each event.

Following the training of the weighting coefficients, data that had not been used

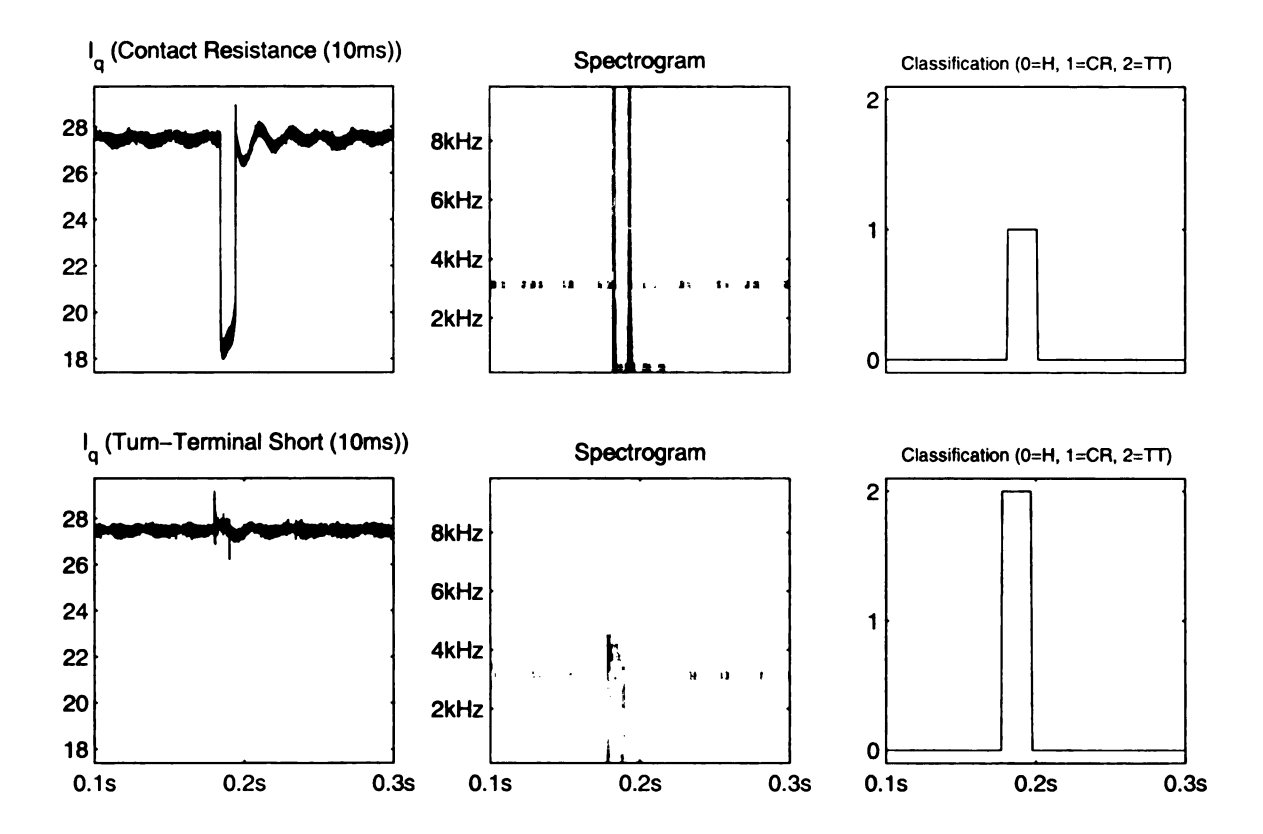


Figure 4.2. Typical Results (Section 4.1.2)

in the training algorithm were tested. Two new data sets from each of the following operating conditions were tested: Healthy; 5ms increased contact resistance; 10ms increased contact resistance; 5ms turn-terminal short; and 10ms turn-terminal short.

The results from two typical test cases are shown in Fig. 4.2. The top row of Fig. 4.2 has results from the increased contact resistance fault. The bottom row has results from the turn-terminal short. The left column shows the measured torque producing component of the current, i_{qs} , for each test case. The center column shows the spectrogram of the data to the left. The right column is the output of the detection and classification algorithm with 0=healthy, 1=increased contact resistance fault, and 2=turn-terminal short.

The performance of the algorithm can be observed in 4.1. The ten tests described above resulted in no false positives. In the two healthy cases, no fault events were de-

Test Description	Number of False Detections	Fault Total / Detected / Classified Correctly	
Healthy	0	0/0/0	
Contact Resistance (5ms)	0	2 / 2 / 2	
Contact Resistance (10ms)	0	2 / 2 / 2	
Turn-Terminal Short (5ms)	0	2 / 2 / 2	
Turn-Terminal Short (10ms)	0	2 / 2 / 2	

Table 4.1. Algorithm Performance (Section 4.1.2)

tected. In the four cases with the increased contact resistance fault, all fault inception and clearing events were identified correctly. In the four cases with the turn-terminal short, all fault inception and clearing events were identified correctly.

4.1.3 Algorithm Based on the STFT Applied to Electrical Faults (Fast Controller Response)

The experimental data in this section was a result of faster controller response than the original experiments, giving improved transient response and less steady state error. Previous experiments have shown that the algorithms developed are generally invariant to fault duration and rotational speed. Two fault durations were investigated, both 5ms and 10ms, and two rotational speeds were explored, both 10% and 15% the no-load speed.

The emphasis of the new experiments is to show invariance to the resistance value used in the increased contact resistance experiments. Increased contact resistance tests were conducted using five resistance values: 2.14pu, 2.80pu, 4.03pu, 6.33pu, and 15.84pu.

The input to the algorithm developed in this section is 25 STFT samples, or 20ms, of the measured q-axis current, i_{qs} . The algorithm has two parts; a detection phase and a classification phase. The detection phase of the algorithm is based on

thresholding on the time marginal of the STFT. The threshold was set at 4% greater than the largest which was observed in all samples from the healthy machine data. If the energy in new test data exceeds this threshold, a fault is considered to exist.

The classification phase was based on linear discriminant analysis. This phase is implemented when the criterion for detection is met. To train the algorithm, thereby determining the weighting coefficients, data were used from eight experiments from each of the following operating conditions: Healthy, increased contact resistance (2.80pu and 6.33pu), and turn-terminal short. The data used were the 25 samples in the STFT corresponding to each event.

Following the training of the weighting coefficients, data that had not been used in the training algorithm were tested. Two data sets from each of the following operating conditions were tested: Healthy, increased contact resistance (2.14pu, 2.80pu, 4.03pu, 6.33pu, and 15.84pu), and turn-terminal short.

The faster controller response has decreased the fault recovery times for both faults explored. This emphasized one of the disadvantages of the STFT, where a tradeoff must be made between time and frequency resolution. In the case of the UDWT, it is possible to get both good time and frequency resolution in the same analysis. The performance of the UDWT algorithm was much better than the performance of the STFT algorithm under the same test conditions.

The results from two typical test cases are shown in Fig. 4.3. The top row of Fig. 4.3 has results from one of the increased contact resistance faults. The bottom row has results from the turn-terminal short. The left column shows the measured torque producing component of the current, i_{qs} , for each test case. The center column shows the spectrogram of the data to the left. The right column is the output of the detection and classification algorithm with 0=healthy, 1=increased contact resistance fault, and 2=turn-terminal short.

The performance of the algorithm can be observed in Table 4.2. The fourteen tests

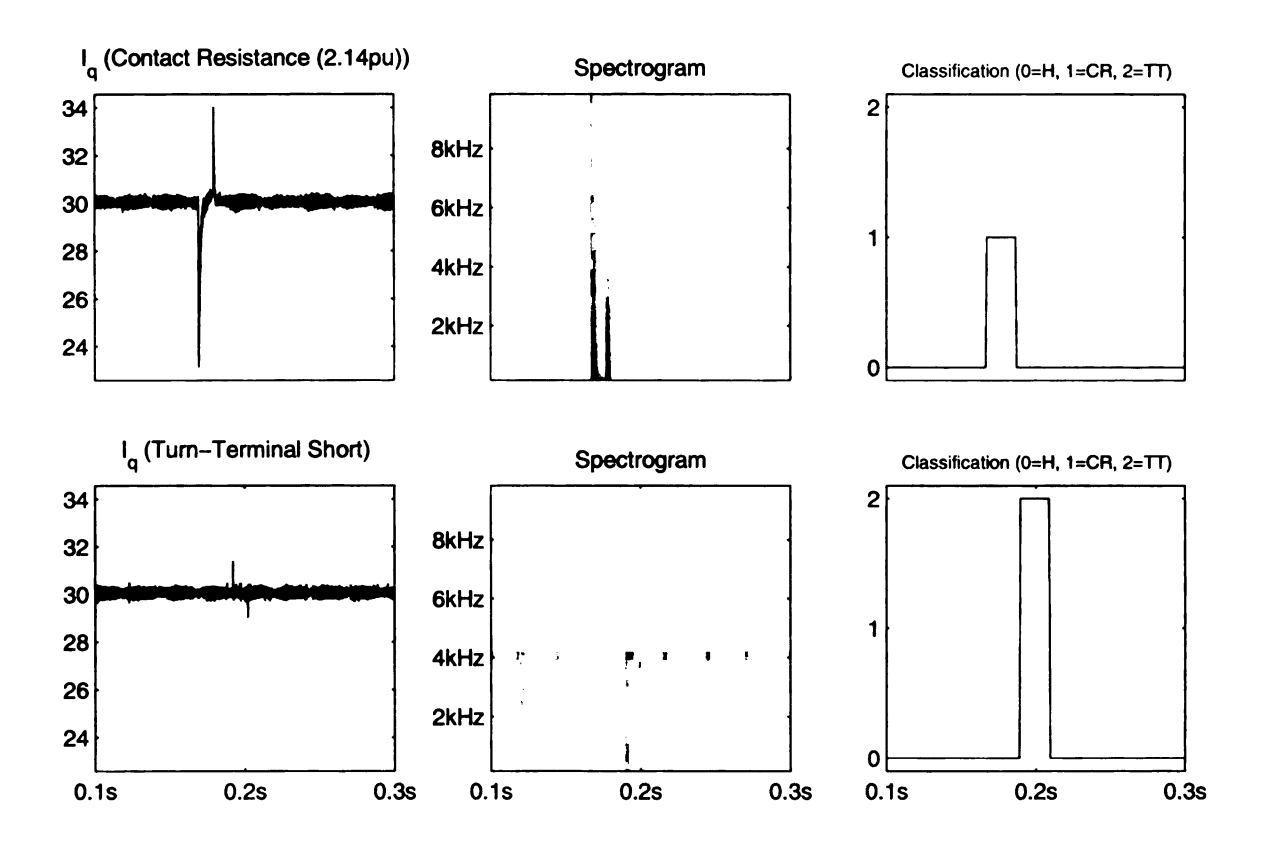


Figure 4.3. Typical Results (Section 4.1.3)

Test Description	Number of False Detections	Fault Total / Detected / Classified Correctly
Healthy	0	0/0/0
Contact Resistance (2.14pu)	0	2 / 2 / 2
Contact Resistance (2.80pu)	0	2 / 2 / 2
Contact Resistance (4.03pu)	0	2 / 2 / 2
Contact Resistance (6.33pu)	0	2 / 2 / 2
Contact Resistance (15.84pu)	0	2 / 2 / 2
Turn-Terminal Short	0	2 / 2 / 2

Table 4.2. Algorithm Performance (Section 4.1.3)

described above resulted in no false positives. Each fault was identified correctly in all twelve tests.

4.1.4 Algorithm Based on the STFT Applied to Electrical Faults with Separate Classification of Fault Inception and Clearing (Slow Controller Response)

The input to the algorithm developed in [48] is 5 STFT samples, or 4ms, of the measured q-axis current, i_{qs} . This time interval is selected to capture the beginning and end of each fault separately. The algorithm has two parts; a detection phase and a classification phase. The detection phase of the algorithm is based on thresholding on the time marginal of the STFT. The threshold was set at 25% greater than the largest which was observed in all samples from the healthy machine data. If the energy in new test data exceeds this threshold, a fault is considered to exist.

The classification phase was based on linear discriminant analysis. This phase is implemented when the criterion for detection is met. Since the fault duration is random, two distinct events were assigned to each intermittent fault; one corresponding to the inception, and the other to the clearing of the fault. The advantage of two separate classes for each fault is invariance to the duration of the fault. Additionally, a postprocessing algorithm to verify that subsequent classification of the beginning and end of the same fault type would further confirm existence of the fault. To train the algorithm, thereby determining the weighting coefficients, data were used from eight experiments from each of the following operating conditions: Healthy, increased contact resistance (5ms and 10ms), and turn-terminal short (5ms and 10ms). The data used were the 5 samples in the STFT corresponding to each event.

Following the training of the weighting coefficients, data that had not been used in the training algorithm were tested. Two new data sets from each of the following

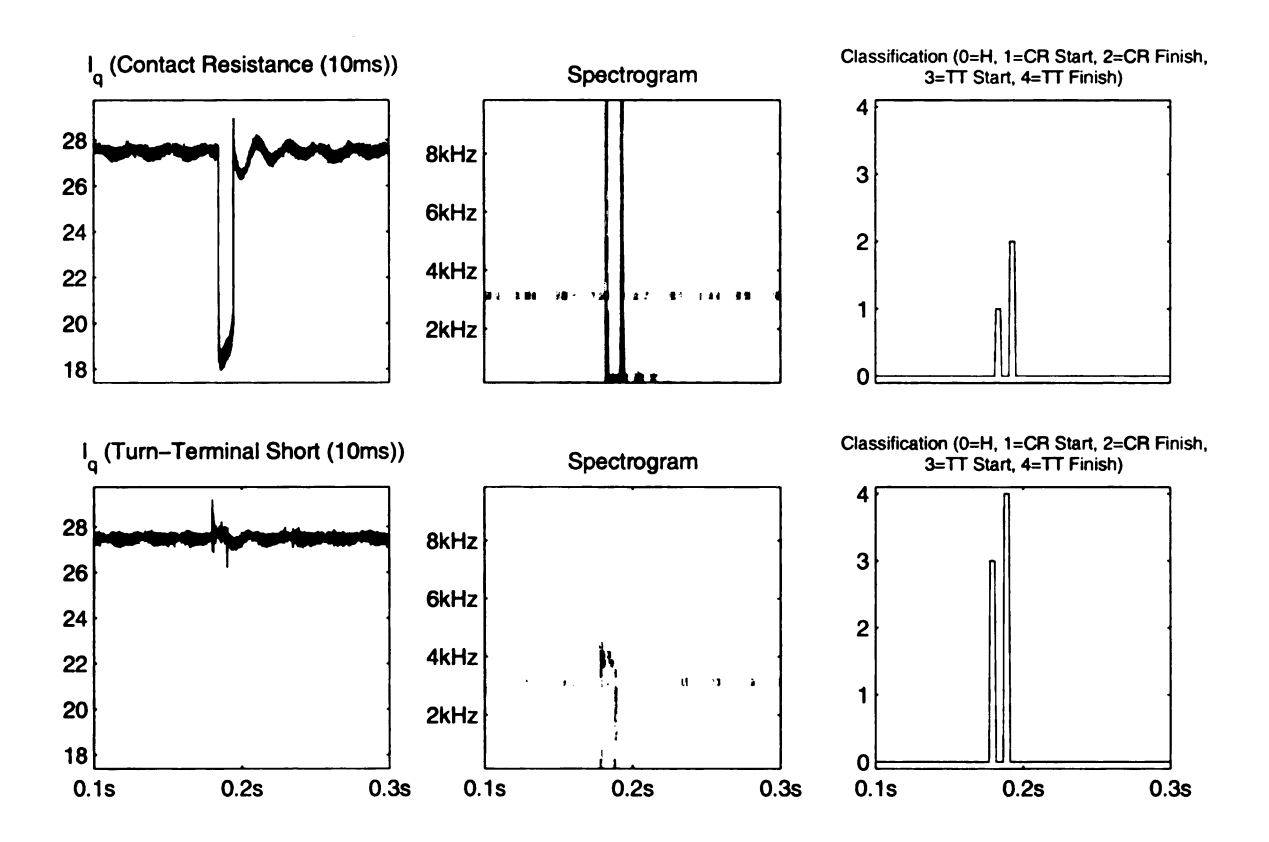


Figure 4.4. Typical Results (Section 4.1.4)

operating conditions were tested: Healthy; 5ms increased contact resistance; 10ms increased contact resistance; 5ms turn-terminal short; and 10ms turn-terminal short.

The results from two typical test cases are shown in Fig. 4.4. The top row of Fig. 4.4 has results from the increased contact resistance fault. The bottom row has results from the turn-terminal short. The left column shows the measured torque producing component of the current, i_{qs} , for each test case. The center column shows the spectrogram of the data to the left. The right column is the output of the detection and classification algorithm with 0=healthy, 1=beginning of increased contact resistance fault, 2=end of increased contact resistance fault, 3=beginning of turn-terminal short, and 4=end of turn-terminal short.

In Fig. 4.4, it can be seen that the magnitude of the STFT coefficients is increased at the points of inception and clearing of the faults. The increased energy at these

Test Description	Number of False Detections	Fault Inception Total / Detected / Classified Correctly	Fault Clearing Total / Detected / Classified Correctly
Healthy	0	0/0/0	0/0/0
Contact Resistance (5ms)	0	2 / 2 / 2	2 / 2 / 2
Contact Resistance (10ms)	0	2 / 2 / 2	2 / 2 / 2
Turn-Terminal Short (5ms)	0	2 / 2 / 2	2 / 2 / 2
Turn-Terminal Short (10ms)	0	2 / 2 / 2	2 / 2 / 2

Table 4.3. Algorithm Performance (Section 4.1.4)

points meets the criterion for detection, and the classification algorithm operates on the STFT coefficients corresponding to 4ms of data at these points. The results shown indicate correct classification of the inception and clearing of both faults explored in this work.

The performance of the algorithm can be observed in 4.3. The ten tests described above resulted in no false positives. In the two healthy cases, no fault events were detected. In the four cases with the increased contact resistance fault, all fault inception and clearing events were identified correctly. In the four cases with the turn-terminal short, all fault inception and clearing events were identified correctly.

4.1.5 Algorithm Based on the STFT Applied to Electrical Faults with Separate Classification of Fault Inception and Clearing (Fast Controller Response)

The experimental data in this section was a result of faster controller response than the original experiments, giving improved transient response and less steady state error. While previous experiments have shown that the algorithms developed are generally invariant to fault duration and rotational speed, the emphasis of the new experiments is to show invariance to the resistance value used in the increased contact resistance experiments. Increased contact resistance tests were conducted using five

resistance values: 2.14pu, 2.80pu, 4.03pu, 6.33pu, and 15.84pu.

The input to the algorithm developed in this section is 5 STFT samples, or 4ms, of the measured q-axis current, i_{qs} . This time interval is selected to capture the beginning and end of each fault separately. The algorithm has two parts; a detection phase and a classification phase. The detection phase of the algorithm is based on thresholding on the time marginal of the STFT. The threshold was set at 4% greater than the largest which was observed in all samples from the healthy machine data. If the energy in new test data exceeds this threshold, a fault is considered to exist.

The classification phase was based on linear discriminant analysis. This phase is implemented when the criterion for detection is met. To train the algorithm, thereby determining the weighting coefficients, data were used from eight experiments from each of the following operating conditions: Healthy, increased contact resistance (2.80pu and 6.33pu), and turn-terminal short. The data used were the 5 samples in the STFT corresponding to each event.

Following the training of the weighting coefficients, data that had not been used in the training algorithm were tested. Two data sets from each of the following operating conditions were tested: Healthy, increased contact resistance (2.14pu, 2.80pu, 4.03pu, 6.33pu, and 15.84pu), and turn-terminal short.

The faster controller response has decreased the fault recovery times for both faults explored. This emphasized one of the disadvantages of the STFT, where a tradeoff must be made between time and frequency resolution. In the case of the UDWT, it is possible to get both good time and frequency resolution in the same analysis. The performance of the UDWT algorithm was much better than the performance of the STFT algorithm under the same test conditions.

The results from two typical test cases are shown in Fig. 4.5. The top row of Fig. 4.5 has results from one of the increased contact resistance faults. The bottom row has results from the turn-terminal short. The left column shows the measured torque

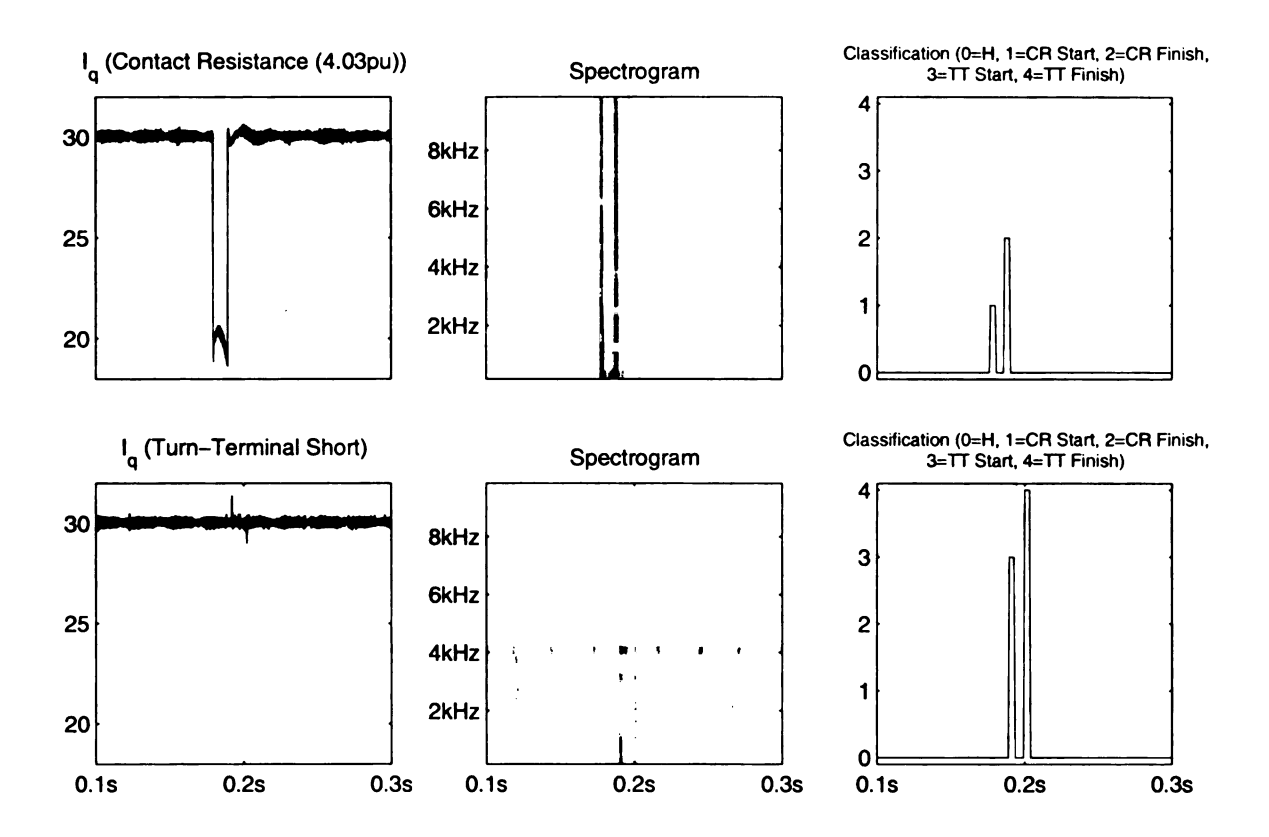


Figure 4.5. Typical Results (Section 4.1.5)

producing component of the current, i_{qs} , for each test case. The center column shows the spectrogram of the data to the left. The right column is the output of the detection and classification algorithm with 0=healthy, 1=beginning of increased contact resistance fault, 2=end of increased contact resistance fault, 3=beginning of turn-terminal short, and 4=end of turn-terminal short.

The performance of the algorithm can be observed in Table 4.4. There were 3 false detections. All fault events were detected, and 15/24 were classified correctly. The faster controller response is attributed to the decrease in accuracy of the STFT based algorithm with the new data compared with the previous data.

Test Description	Number of False Detections	Fault Inception Total / Detected / Classified Correctly	Fault Clearing Total / Detected / Classified Correctly
Healthy	0	0/0/0	0/0/0
Contact Resistance (2.14pu)	0	2 / 2 / 2	2 / 2 / 0
Contact Resistance (2.80pu)	1	2 / 2 / 2	2 / 2 / 0
Contact Resistance (4.03pu)	0	2 / 2 / 1	2 / 2 / 2
Contact Resistance (6.33pu)	0	2 / 2 / 1	2 / 2 / 1
Contact Resistance (15.84pu)	2	2 / 2 / 0	2 / 2 / 2
Turn-Terminal Short	0	2 / 2 / 2	2 / 2 / 2

Table 4.4. Algorithm Performance (Section 4.1.5)

4.1.6 Algorithm Based on the STFT Applied to Mechanical Faults (Fast Controller Response)

The input to the algorithm developed in this section is 12 STFT samples, or 9.6ms, of the measured q-axis current, i_{qs} . The algorithm has two parts; a detection phase and a classification phase. The detection phase of the algorithm is based on thresholding on the time marginal of the STFT. The threshold was set at 80% greater than the largest which was observed in all samples from healthy gears or with one missing tooth. Based on the contact ratio of the gears chosen for this project, the difference in the current between the healthy case and the case with one missing tooth was insignificant. If the energy in new test data exceeds these thresholds, a fault is considered to exist.

The classification phase was based on linear discriminant analysis. This phase is implemented when the criterion for detection is met. To train the algorithm, thereby determining the weighting coefficients, data were used from 9 experiments, corresponding to 26 fault events, to train the algorithms for each fault. The data used were the 12 samples in the STFT corresponding to each event.

Following the training of the weighting coefficients, data that had not been used in the training algorithm were tested. One new data set from each of the following operating conditions were tested: One tooth missing and its adjacent tooth severely

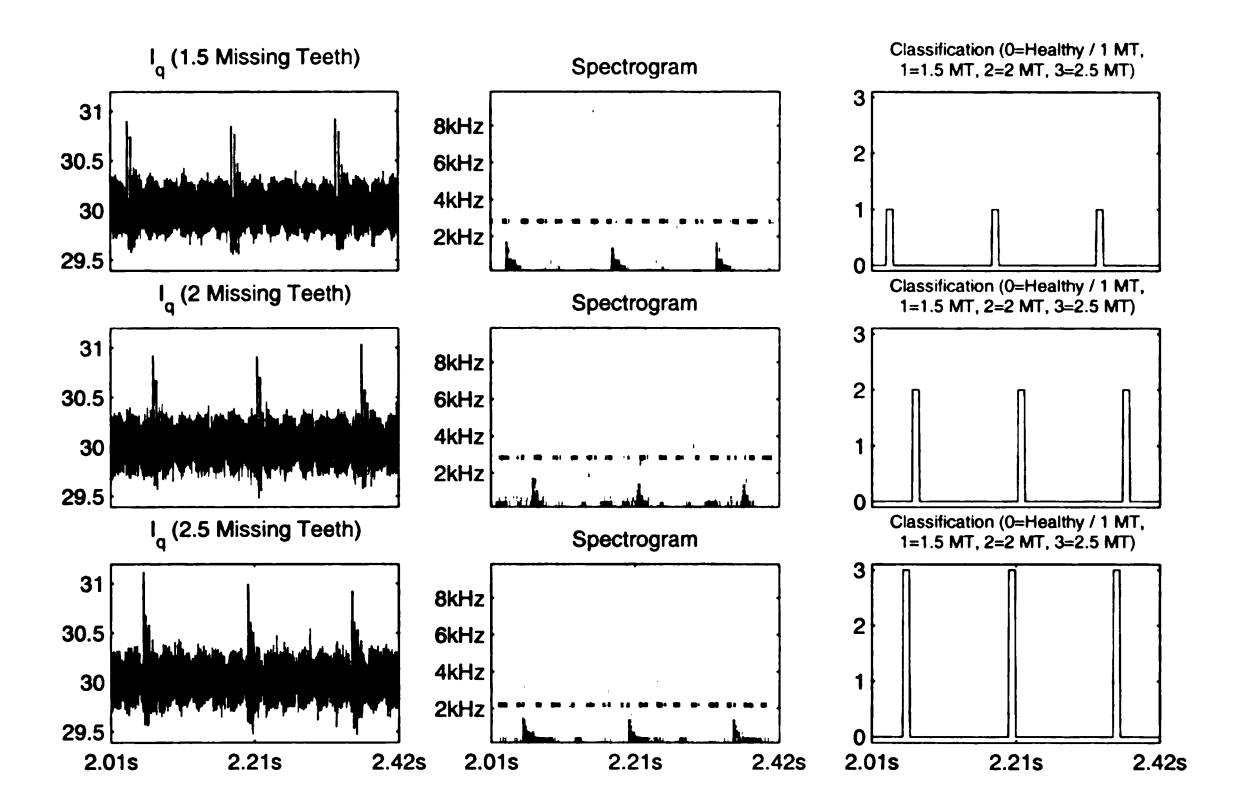


Figure 4.6. Experimental Results (Section 4.1.6)

worn; two adjacent teeth missing; and two adjacent teeth missing and their adjacent tooth severely worn. Each of these data sets contained three fault events.

The results from the three test cases are shown in Fig. 4.6. The left column of Fig. 4.6 shows the measured torque producing component of the current, i_{qs} , for each test case. The center column shows the spectrogram of the data to the left. The right column is the output of the detection and classification algorithm with 0=healthy / one tooth missing, 1=one tooth missing and its adjacent tooth severely worn, 2=two adjacent teeth missing, and 3=two adjacent teeth missing with their adjacent tooth severely worn.

The performance of the algorithm can be observed in Table 4.5. The three tests described above resulted in no false positives. All nine fault events were identified correctly.

Test Description	Number of False Detections	Fault Total / Detected / Classified Correctly
Healthy	0	0/0/0
1 Missing Tooth	0	0/0/0
1.5 Missing Teeth	0	3 / 3 / 3
2 Missing Teeth	0	3/3/3
2.5 Missing Teeth	0	3 / 3 / 3

Table 4.5. Algorithm Performance (Section 4.1.6)

4.1.7 Algorithm Based on the DWT

The use of the DWT was explored in this work, however due to the non-shift-invariant nature of the DWT, the accuracy of the detection phase of the algorithm was poor. The presence of a fault could be detected, however, it was difficult to pinpoint exactly the time of inception and clearing. Poor classification performance was also a result of this limitation of the DWT.

To illustrate this, an attempt at detecting the presence of a fault, as well as determining precisely its time of inception and clearing, is explored. The energy in the DWT of a signal is analyzed, which is defined as the sum of the square of the DWT coefficients corresponding to a particular time instant. An example energy calculation, based on the coefficients shown in in Fig. 2.10, at t_5 is defined as $E(t_5) = d_{2,2}^2 + d_{1,0}^2 + d_{0,0}^2$.

Through inspection of the DWT energy, it can been seen that the presence of a fault can be detected, but it is difficult to determine its exact time of inception and clearing. This is due to the fact that the DWT has poor time resolution at low frequency scales.

In Fig. 4.7, i_{qs} from a test with a 4.03pu intermittent increased contact resistance fault initiated at 95% of the peak phase current, with a duration of 10ms, running at 1/10 the no-load speed is shown.

The DWT of the current is shown in Fig. 4.8. Here, the plots from top to bottom

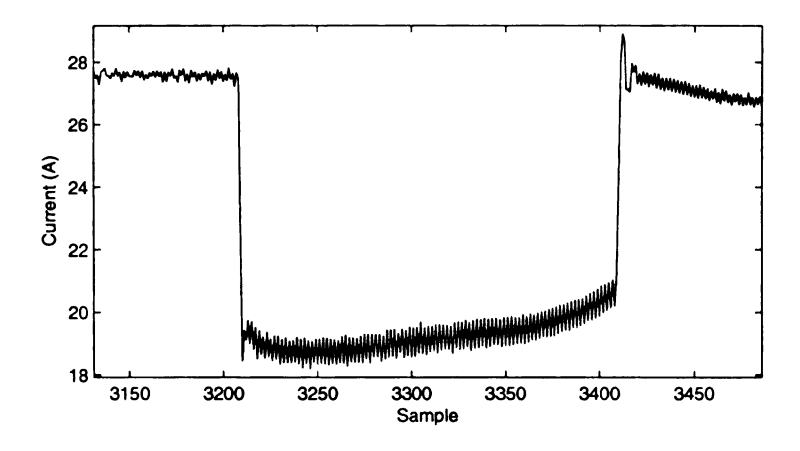


Figure 4.7. Original Signal

are scales 5–0. It can be seen that the number of coefficients decreases by a factor of 2 at each scale due to downsampling.

Finally, the energy of the DWT is shown in Fig. 4.9. The vertical dashed lines in the figure designate the inception and the clearing of the fault respectively. It can be seen that by using thresholding on the energy of the DWT as a criterion for fault detection, it is difficult to precisely identify the time of fault inception and clearing.

4.1.8 Algorithm Based on the UDWT Applied to Electrical Faults (Slow Controller Response)

The input to one of the algorithms developed in [49] is 400 UDWT samples, or 20ms, of the measured q-axis current, i_{qs} . For this analysis, the Daubechies D4 mother wavelet was used and decomposition was performed to 6 levels. The algorithm has two parts; a detection phase and a classification phase. The detection phase of the algorithm is based on thresholding on the weighted energy in the UDWT. The threshold was set at 12% greater than the largest which was observed in all samples from the healthy machine data. If the weighted energy in new test data exceeds this threshold, a fault is considered to exist.

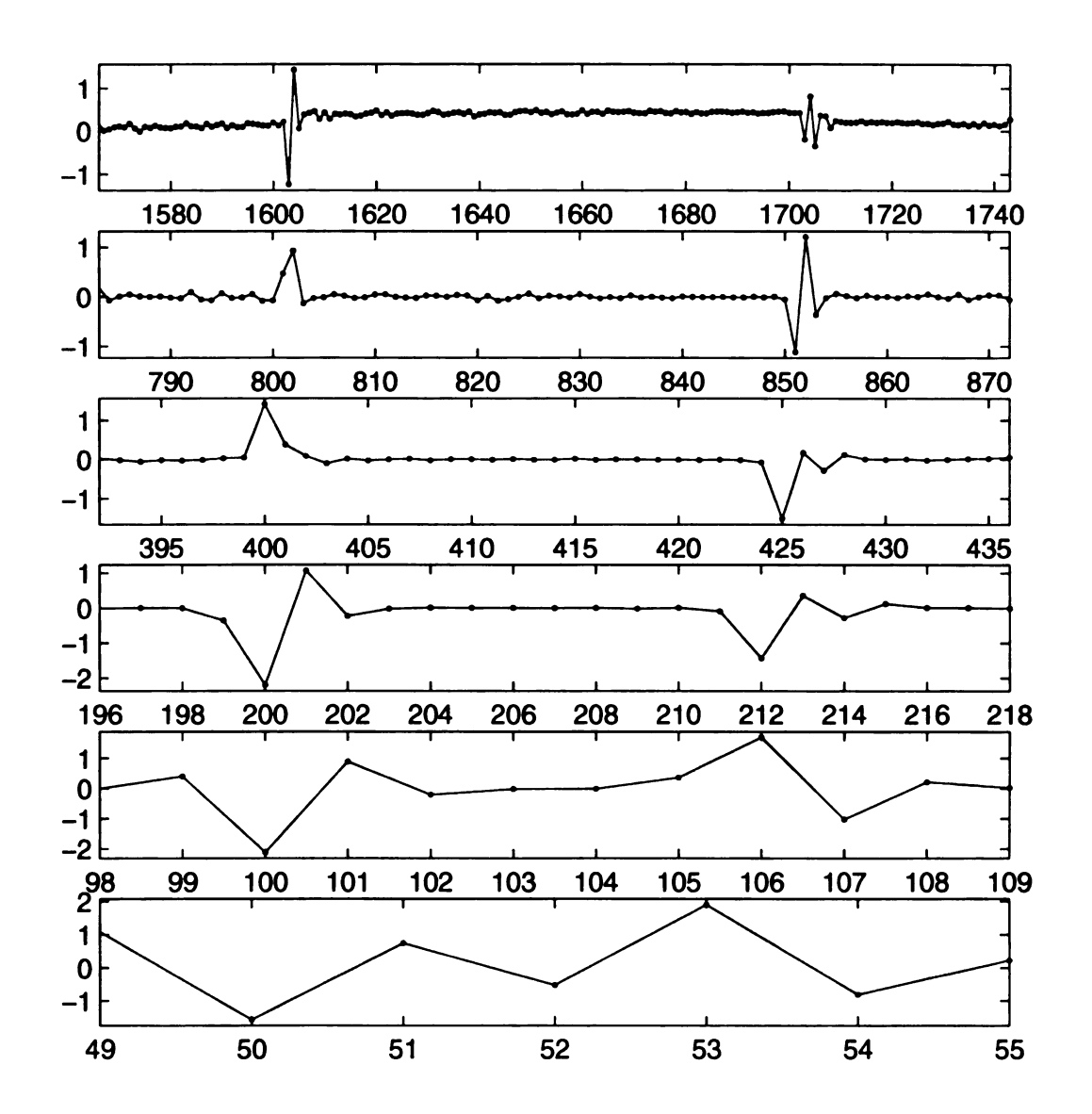


Figure 4.8. DWT of the Original Signal

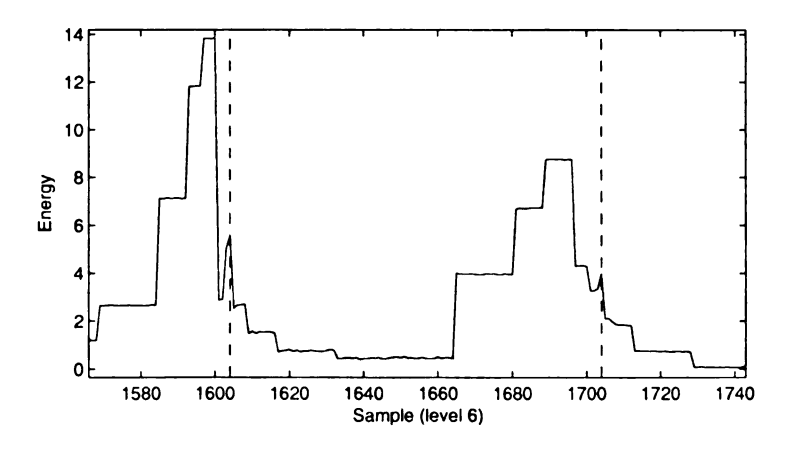


Figure 4.9. Energy in the DWT of the Original Signal

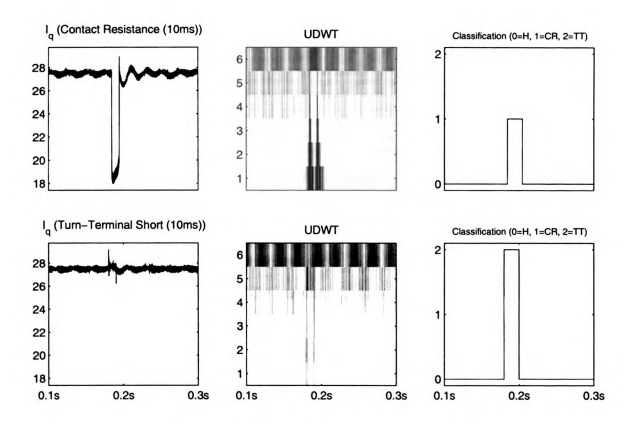


Figure 4.10. Typical Results (Section 4.1.8)

The classification phase was based on linear discriminant analysis. This phase is implemented when the criterion for detection is met. To train the algorithm, thereby determining the weighting coefficients, data were used from eight experiments from each of the following operating conditions: Healthy, increased contact resistance (5ms and 10ms), and turn-terminal short (5ms and 10ms). The data used were the 400 samples in the UDWT corresponding to each event.

Following the training of the weighting coefficients, data that had not been used in the training algorithm were tested. Two data sets from each of the following operating conditions were tested: Healthy; 5ms increased contact resistance; 10ms increased contact resistance; 5ms turn-terminal short; and 10ms turn-terminal short.

The results from two typical test cases are shown in Fig. 4.10. The top row of Fig. 4.10 has results from the increased contact resistance fault. The bottom

Test Description	Number of False Detections	Fault Total / Detected / Classified Correctly
Healthy	0	0/0/0
Contact Resistance (5ms)	0	2 / 2 / 2
Contact Resistance (10ms)	0	2 / 2 / 2
Turn-Terminal Short (5ms)	0	2 / 2 / 2
Turn-Terminal Short (10ms)	0	2 / 2 / 2

Table 4.6. Algorithm Performance (Section 4.1.8)

row has results from the turn-terminal short. The left column shows the measured torque producing component of the current, i_{qs} , for each test case. The center column shows the spectrogram of the data to the left. The right column is the output of the detection and classification algorithm with 0=healthy, 1=increased contact resistance fault, and 2=turn-terminal short.

The performance of the algorithm can be observed in Table 4.6. The ten tests described above resulted in no false positives. Each fault was identified correctly in all eight tests.

4.1.9 Algorithm Based on the UDWT Applied to Electrical Faults (Fast Controller Response)

The experimental data in this section was a result of faster controller response than the original experiments, giving improved transient response and less steady state error. While previous experiments have shown that the algorithms developed are generally invariant to fault duration and rotational speed, the emphasis of the new experiments is to show invariance to the resistance value used in the increased contact resistance experiments. Increased contact resistance tests were conducted using five resistance values: 2.14pu, 2.80pu, 4.03pu, 6.33pu, and 15.84pu.

The input to the algorithm developed in this section is 400 UDWT samples, or

20ms, of the measured q-axis current, i_{qs} . For this analysis, the Daubechies D4 mother wavelet was used and decomposition was performed to 6 levels. The algorithm has two parts; a detection phase and a classification phase. The detection phase of the algorithm is based on thresholding on the energy in the UDWT. The threshold was set at 50% greater than the largest which was observed in all samples from the healthy machine data. If the energy in new test data exceeds this threshold, a fault is considered to exist.

The classification phase was based on linear discriminant analysis. This phase is implemented when the criterion for detection is met. To train the algorithm, thereby determining the weighting coefficients, data were used from eight experiments from each of the following operating conditions: Healthy, increased contact resistance (2.80pu and 6.33pu), and turn-terminal short. The data used were the 64 samples in the UDWT corresponding to each event.

Following the training of the weighting coefficients, data that had not been used in the training algorithm were tested. Two data sets from each of the following operating conditions were tested: Healthy, increased contact resistance (2.14pu, 2.80pu, 4.03pu, 6.33pu, and 15.84pu), and turn-terminal short.

The faster controller response has decreased the fault recovery times for both faults explored. This emphasized one of the disadvantages of the STFT, where a tradeoff must be made between time and frequency resolution. In the case of the UDWT, it is possible to get both good time and frequency resolution in the same analysis. The performance of the UDWT algorithm was much better than the performance of the STFT algorithm under the same test conditions.

The results from two typical test cases are shown in Fig. 4.11. The top row of Fig. 4.11 has results from one of the increased contact resistance faults. The bottom row has results from the turn-terminal short. The left column shows the measured torque producing component of the current, i_{qs} , for each test case. The center column

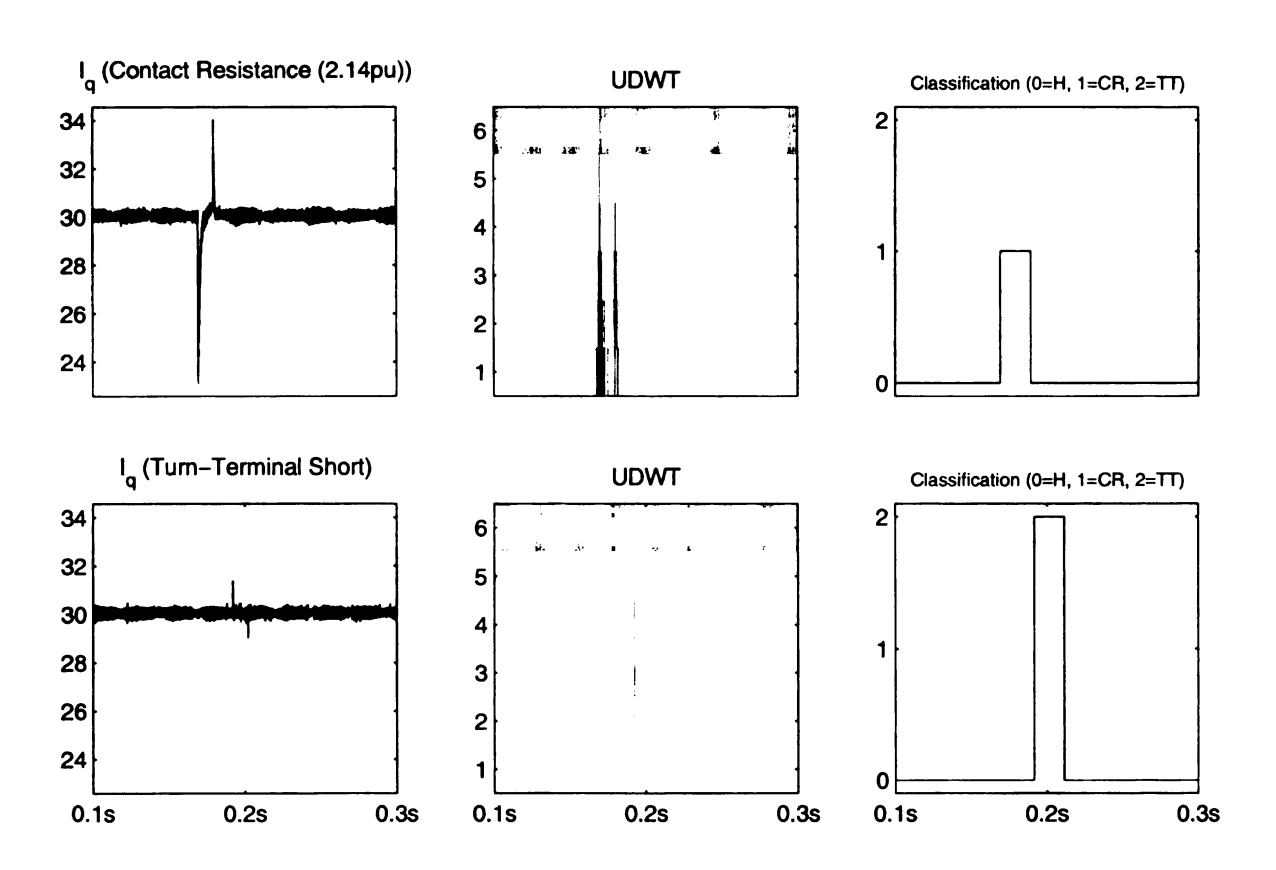


Figure 4.11. Typical Results (Section 4.1.9)

Test Description	Number of False Detections	Fault Total / Detected / Classified Correctly
Healthy	0	0/0/0
Contact Resistance (2.14pu)	0	2 / 2 / 2
Contact Resistance (2.80pu)	0	2 / 2 / 2
Contact Resistance (4.03pu)	0	2 / 2 / 2
Contact Resistance (6.33pu)	0	2 / 2 / 2
Contact Resistance (15.84pu)	0	2 / 2 / 2
Turn-Terminal Short	0	2 / 2 / 2

Table 4.7. Algorithm Performance (Section 4.1.9)

shows the spectrogram of the data to the left. The right column is the output of the detection and classification algorithm with 0=healthy, 1=increased contact resistance fault, and 2=turn-terminal short.

The performance of the algorithm can be observed in Table 4.7. The fourteen tests described above resulted in no false positives. Each fault was identified correctly in all twelve tests.

4.1.10 Algorithm Based on the UDWT Applied to Electrical Faults with Separate Classification of Fault Inception and Clearing (Slow Controller Response)

The input to the algorithm developed in [50] is 64 UDWT samples, or 3.2ms, of the measured q-axis current, i_{qs} . This time interval is selected to capture the beginning and end of each fault separately. For this analysis, the Daubechies D4 mother wavelet was used and decomposition was performed to 6 levels. The algorithm has two parts; a detection phase and a classification phase. The detection phase of the algorithm is based on thresholding on the weighted energy in the UDWT. The threshold was set at 40% greater than the largest which was observed in all samples from the healthy machine data. If the weighted energy in new test data exceeds this threshold, a fault

is considered to exist.

The classification phase was based on linear discriminant analysis. This phase is implemented when the criterion for detection is met. Since the fault duration is random, two distinct events were assigned to each intermittent fault; one corresponding to the inception, and the other to the clearing of the fault. The advantage of two separate classes for each fault is invariance to the duration of the fault. Additionally, a postprocessing algorithm to verify that subsequent classification of the beginning and end of the same fault type would further confirm existence of the fault. To train the algorithm, thereby determining the weighting coefficients, data were used from eight experiments from each of the following operating conditions: Healthy, increased contact resistance (5ms and 10ms), and turn-terminal short (5ms and 10ms). The data used were the 64 samples in the UDWT corresponding to each event.

Following the training of the weighting coefficients, data that had not been used in the training algorithm were tested. Two data sets from each of the following operating conditions were tested: Healthy; 5ms increased contact resistance; 10ms increased contact resistance; 5ms turn-terminal short; and 10ms turn-terminal short.

The results from two typical test cases are shown in Fig. 4.12. The top row of Fig. 4.12 has results from the increased contact resistance fault. The bottom row has results from the turn-terminal short. The left column shows the measured torque producing component of the current, i_{qs} , for each test case. The center column shows the spectrogram of the data to the left. The right column is the output of the detection and classification algorithm with 0=healthy, 1=beginning of increased contact resistance fault, 2=end of increased contact resistance fault, 3=beginning of turn-terminal short, and 4=end of turn-terminal short.

In Fig. 4.12, it can be seen that the amplitude of the UDWT coefficients is increased at the points of inception and clearing of the faults. The increased energy at these points meets the criterion for detection, and the classification algorithm

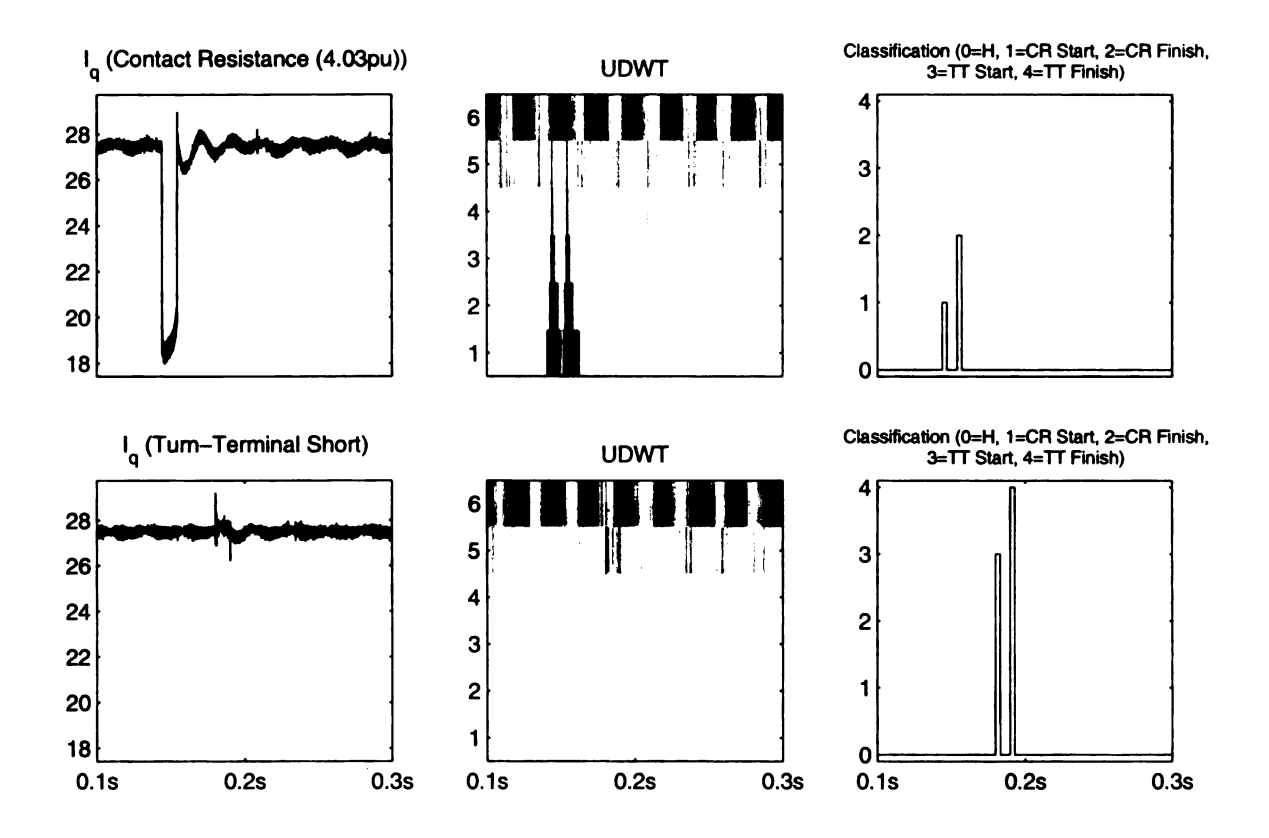


Figure 4.12. Typical Results (Section 4.1.10)

operates on the UDWT coefficients corresponding to 3.2ms of data at these points. The results shown indicate correct classification of the inception and clearing of both faults explored in this work.

The performance of the algorithm can be observed in Table 4.8. The ten tests described above resulted in no false positives and one false negative. In the two healthy cases, no fault events were detected. In the four cases with the increased contact resistance fault, all fault inception and clearing events were identified correctly. In the four cases with the turn-terminal short, three of the four fault inception events were identified correctly, and the fourth did not meet the criterion for detection; all four fault clearing events were identified correctly.

Test Description	Number of False Detections	Fault Inception Total / Detected / Classified Correctly	Fault Clearing Total / Detected / Classified Correctly
Healthy	0	0/0/0	0/0/0
Contact Resistance (5ms)	0	2 / 2 / 2	2 / 2 / 2
Contact Resistance (10ms)	0	2 / 2 / 2	2 / 2 / 2
Turn-Terminal Short (5ms)	0	2 / 1 / 1	2 / 2 / 2
Turn-Terminal Short (10ms)	0	2 / 2 / 2	2 / 2 / 2

Table 4.8. Algorithm Performance (Section 4.1.10)

4.1.11 Algorithm Based on the UDWT Applied to Electrical Faults with Separate Classification of Fault Inception and Clearing (Fast Controller Response)

The experimental data in this section was a result of faster controller response than the original experiments, giving improved transient response and less steady state error. While previous experiments have shown that the algorithms developed are generally invariant to fault duration and rotational speed, the emphasis of the new experiments is to show invariance to the resistance value used in the increased contact resistance experiments. Increased contact resistance tests were conducted using five resistance values: 2.14pu, 2.80pu, 4.03pu, 6.33pu, and 15.84pu.

The input to the algorithm developed in this section is 64 UDWT samples, or 3.2ms, of the measured q-axis current, i_{qs} . This time interval is selected to capture the beginning and end of each fault separately. For this analysis, the Daubechies D4 mother wavelet was used and decomposition was performed to 6 levels. The algorithm has two parts; a detection phase and a classification phase. The detection phase of the algorithm is based on thresholding on the energy in the UDWT. The threshold was set at 50% greater than the largest which was observed in all samples from the healthy machine data. If the energy in new test data exceeds this threshold, a fault is considered to exist.

The classification phase was based on linear discriminant analysis. This phase is implemented when the criterion for detection is met. To train the algorithm, thereby determining the weighting coefficients, data were used from eight experiments from each of the following operating conditions: Healthy, increased contact resistance (2.80pu and 6.33pu), and turn-terminal short. The data used were the 64 samples in the UDWT corresponding to each event.

Following the training of the weighting coefficients, data that had not been used in the training algorithm were tested. Two data sets from each of the following operating conditions were tested: Healthy, increased contact resistance (2.14pu, 2.80pu, 4.03pu, 6.33pu, and 15.84pu), and turn-terminal short.

The faster controller response has decreased the fault recovery times for both faults explored. This emphasized one of the disadvantages of the STFT, where a tradeoff must be made between time and frequency resolution. In the case of the UDWT, it is possible to get both good time and frequency resolution in the same analysis. The performance of the UDWT algorithm was much better than the performance of the STFT algorithm under the same test conditions.

The results from two typical test cases are shown in Fig. 4.13. The top row of Fig. 4.13 has results from one of the increased contact resistance faults. The bottom row has results from the turn-terminal short. The left column shows the measured torque producing component of the current, i_{qs} , for each test case. The center column shows the spectrogram of the data to the left. The right column is the output of the detection and classification algorithm with 0=healthy, 1=beginning of increased contact resistance fault, 2=end of increased contact resistance fault, 3=beginning of turn-terminal short, and 4=end of turn-terminal short.

The performance of the algorithm can be observed in Table 4.9. There were no false detections. All fault events were detected and classified correctly except for the clearing of one of the 2.14pu increased contact resistance faults. The 2.14pu

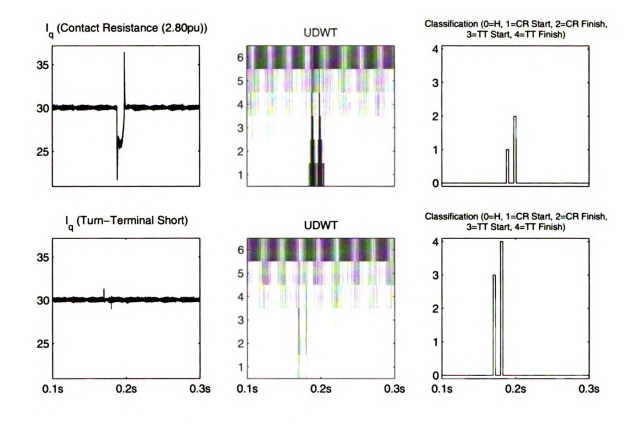


Figure 4.13. Typical Results (Section 4.1.11)

Test Description	Number of False Detections	Fault Inception Total / Detected / Classified Correctly	Fault Clearing Total / Detected / Classified Correctly
Healthy	0	0/0/0	0/0/0
Contact Resistance (2.14pu)	0	2 / 2 / 2	2 / 2 / 1
Contact Resistance (2.80pu)	0	2 / 2 / 2	2 / 2 / 2
Contact Resistance (4.03pu)	0	2/2/2	2/2/2
Contact Resistance (6.33pu)	0	2 / 2 / 2	2 / 2 / 2
Contact Resistance (15.84pu)	0	2 / 2 / 2	2 / 2 / 2
Turn-Terminal Short	0	2/2/2	2 / 2 / 2

Table 4.9. Algorithm Performance (Section 4.1.11)

increased contact resistance fault, however, is outside of the range of values for which the algorithm was trained.

4.1.12 Algorithm Based on the UDWT Applied to Mechanical Faults (Fast Controller Response)

The input to one of the algorithms developed in [49] is 128 UDWT samples, or 6.4ms, of the measured q-axis current, i_{qs} . For this analysis, the Daubechies D4 mother wavelet was used and decomposition was performed to 6 levels. The algorithm has two parts; a detection phase and a classification phase. The detection phase of the algorithm is based on thresholding on the energy in the UDWT. The threshold was set at 80% greater than the largest which was observed in all samples from healthy gears or with one missing tooth. Based on the contact ratio of the gears chosen for this project, the difference in the current between the healthy case and the case with one missing tooth was insignificant. If the energy in new test data exceeds these thresholds, a fault is considered to exist.

The classification phase was based on linear discriminant analysis. This phase is implemented when the criterion for detection is met. To train the algorithm, thereby determining the weighting coefficients, data were used from 9 experiments, corresponding to 26 fault events, to train the algorithms for each fault. The data used were the 128 samples in the UDWT corresponding to each event.

Following the training of the weighting coefficients, data that had not been used in the training algorithm were tested. One new data set from each of the following operating conditions were tested: One tooth missing and its adjacent tooth severely worn; two adjacent teeth missing; and two adjacent teeth missing and their adjacent tooth severely worn. Each of these data sets contained three fault events.

The results from the three test cases are shown in Fig. 4.14. The left column of Fig. 4.14 shows the measured torque producing component of the current, i_{qs} , for

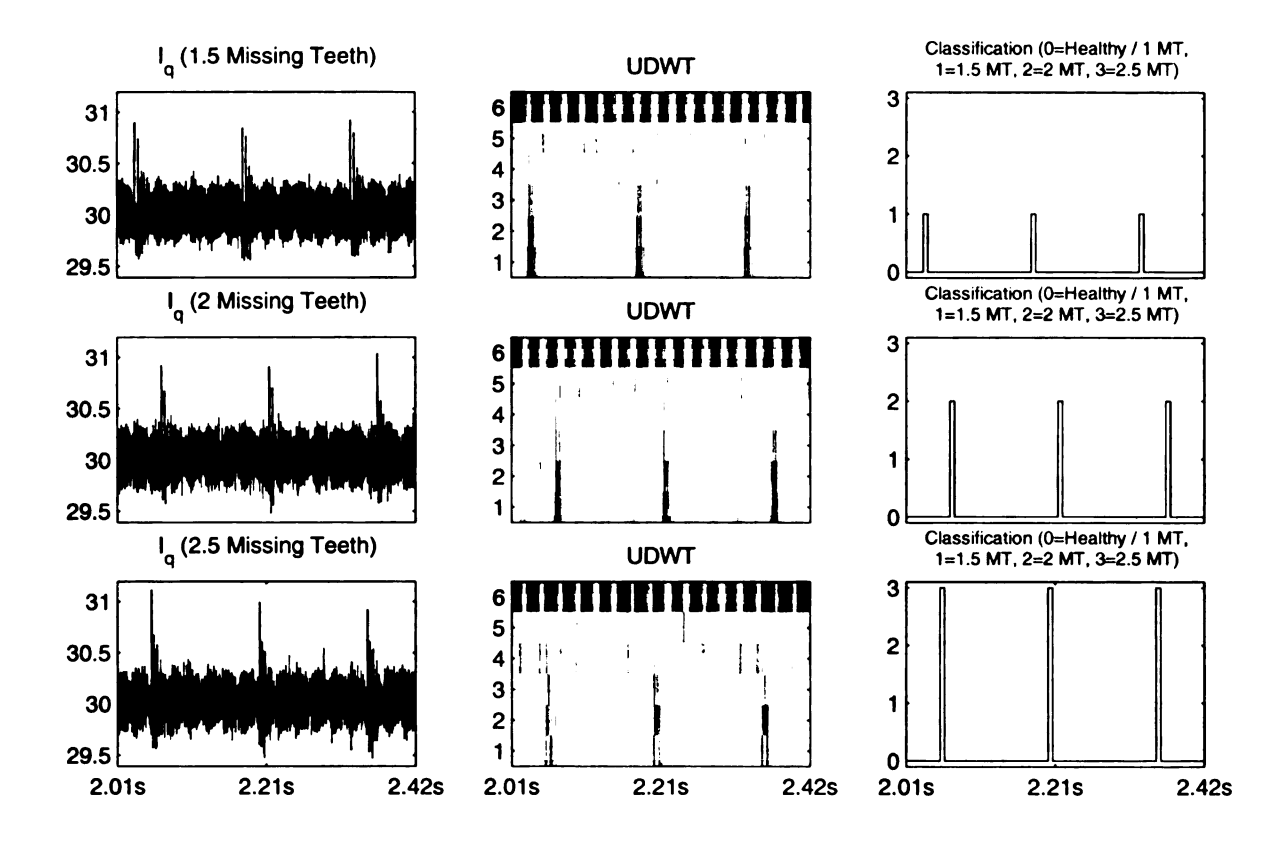


Figure 4.14. Experimental Results (Section 4.1.12)

each test case. The center column shows the UDWT for the data to the left. The right column is the output of the detection and classification algorithm with 0=healthy / one tooth missing, 1=one tooth missing and its adjacent tooth severely worn, 2=two adjacent teeth missing, and 3=two adjacent teeth missing with their adjacent tooth severely worn.

The performance of the algorithm can be observed in Table 4.10. The three tests described above resulted in no false positives. All nine fault events were identified correctly.

Test Description	Number of False Detections	Fault Total / Detected / Classified Correctly
Healthy	0	0/0/0
1 Missing Tooth	0	0/0/0
1.5 Missing Teeth	0	3/3/3
2 Missing Teeth	0	3 / 3 / 3
2.5 Missing Teeth	0	3 / 3 / 3

Table 4.10. Algorithm Performance (Section 4.1.12)

4.2 Finite Element Analysis

Faults in load, power electronics, and magnetics were investigated through the use of FEA. Load faults caused by friction or bad bearings can be introduced by altering the speed in the case of imposed angular speed, or by altering the friction coefficient in the case of a kinematic coupling. Load faults caused by eccentricities of the rotor can be introduced by altering the geometry of the machine. In the case of a static eccentricity, the position of the stator can be altered, and in the case of a dynamic eccentricity, the position of the rotor can be changed.

Power electronics faults caused by intermittent connections can be introduced by adding switches in the inverter circuit. Turn-to-turn, turn-to-ground, or other shorts between windings can be introduced by adding switches in the connection diagram. Switches with additional delays can be introduced by modifying the control strategy, and various other switch anomalies, e.g. changing $R_{DS(on)}$ during the simulation, can be introduced using a Fortran subroutine or Simulink.

Magnetic faults caused by broken or cracked magnets can be introduced by removing a piece of the magnet in the geometry. Partial demagnetization can be introduced by changing the properties of one of the permanent magnets in the simulation.

FEA results using a commercial package, Flux2D, were considered for use in training the detection and classification algorithms; however the spectrum of the prelim-

inary FEA results was significantly different than that of the experimental results. The use of FEA would allow for increased flexibility, giving more training samples, for the faults explored. Fault detection approaches based on results from FEA were introduced in [4,13], however the faults of interest were limited to low-frequency phenomena (i.e. broken rotor bars, rotor eccentricities, and defective magnets), compared to the faults studied in this work. Improvements in the FEA model are expected to decrease the difference between the results, however, there are still phenomena which will be difficult to model. Examples include the switching in a PWM inverter, requiring very small time steps, as well as the inclusion of required parasitic capacitances.

4.2.1 Time Step

Flux2D has a limitation for problems coupled to a circuit, in that the time step used by the solver is fixed, so care must be taken to choose an appropriate time step. To validate that the time step chosen is small enough, a problem must be solved with the desired time step, as well as with a smaller factor of the time step. If results for parameters of interest at overlapping time steps are reasonably close, the desired time step is adequate.

4.2.2 Current Sources vs. Voltage Sources

The parameters which are affected by a fault can be determined by the type of sources used in the circuit for FEA, and the time constant of a fault compared with the speed of the control loops in the system.

If current sources, or a current source inverter using voltage sources controlled by PWM (with a current control loop much faster than that of the faults of interest) are used, fault information will be present in the voltages only. If a current source inverter using voltage sources controlled by PWM (with a typical control loop, or one

which is slower than that of the faults of interest) is used, fault information will be present in both the voltages and currents.

Similar conclusions can be made about the DC link voltages and currents. In the case of a stiff DC link voltage, fault information will be present in the DC link current only. In the case of a soft DC link voltage, fault information will be present in both the DC link voltage and current.

Initial FEA simulations used current sources rather than voltage sources controlled by PWM. This was done in order to observe how a fault manifests itself in the line-line voltages of a machine, since in this case, the currents were not affected by faults. Compared with a circuit using voltage sources controlled by PWM, this makes the following assumptions:

- 1. The high frequencies in the voltage resulting from PWM control are not present;
- 2. The DC bus voltage is stiff, or rather large enough to maintain the desired current in the presence of a short circuit; and
- 3. The delays inherent in a voltage source controller maintaining a desired current are infinitely small.

4.2.3 Measurement Resistors

Another known issue with Flux2D was related to the addition of resistors to measure line-neutral voltages of the machine. This was done since, with Flux2D, voltages in a circuit can only be measured across a component. Initially, the resistance value for these measurement resistors was set to $1M\Omega$. Line-neutral voltages using $1M\Omega$ measurement resistors were compared to those using $100k\Omega$ and $10k\Omega$ resistors but each was found to be slightly different. This can be attributed to the fact that the values of the measurement resistors are several orders of magnitude greater than the coils in the circuit. For this reason, these measurement resistors were eliminated

from the circuit and line-line voltages across the current sources were analyzed instead of line-neutral voltages. Additionally, line-neutral voltages are not available in the experiment since the neutral is not accessible on the test motor.

CHAPTER 5

Experiment Design

A block diagram for the experimental setup is shown in Fig. 5.1. A PC running RT-Linux was used as the controller for this project. The PC is a good choice compared with a DSP in terms of cost, CPU power, and memory capacity. A fundamental limitation of the PC, however, is the limited I/O capability. To remedy this, a custom Xilinx FPGA based I/O board was developed. The I/O board has 12 A/D input channels (12-bit, +/-10V range) and inputs for an encoder. The encoder inputs accept dual quadrature channels and an index pulse in either differential or single-ended configurations. The board processes the encoder counts and stores absolute position in a 12-bit counter. There are 12 digital outputs which can be configured for PWM

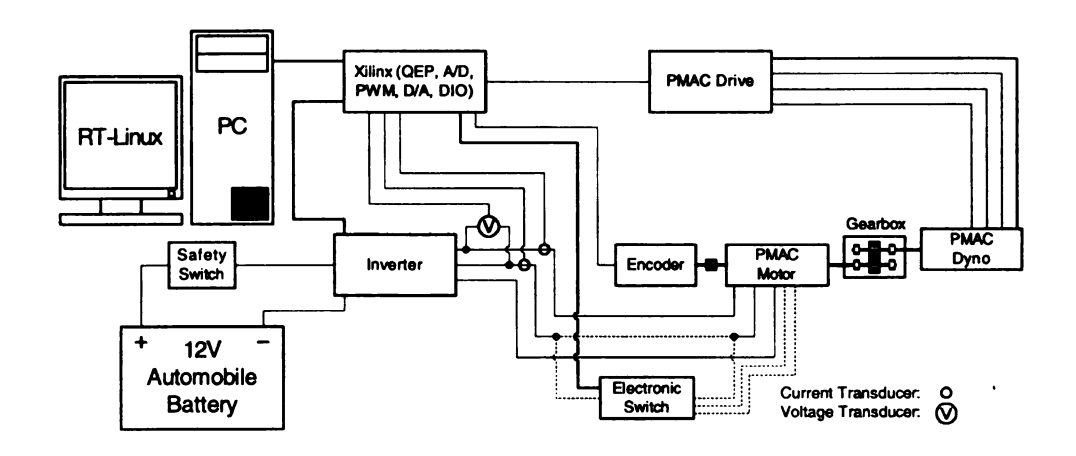


Figure 5.1. Experimental Setup Block Diagram

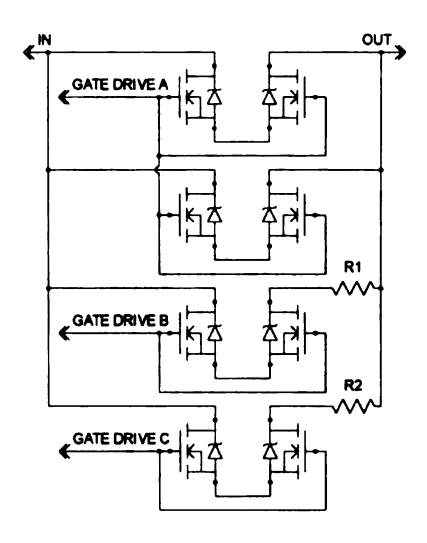


Figure 5.2. Electronic Switch

(2500 counts at 20kHz) and 4 D/A outputs (12-bit, +/-5V range). Communication between the I/O board and the PC is via the EPP parallel port.

Two phase currents were measured using current transducers with rated accuracy of 0.45% and bandwidth of 0-200kHz. A single line-line voltage for use in the initial position calibration was measured as well.

A quadrature encoder with 1024 counts per revolution (4096 for quadrature) and an index pulse was used to measure the rotor position.

A bi-directional analog switch was designed to initiate electronic faults in the stator. This switch is reconfigurable as shown by the dotted lines in Fig. 5.1. It can be configured to initiate either the intermittent increased contact resistance fault or the turn-terminal short. A circuit diagram for the electronic switch is shown in Fig. 5.2. $R_{DS(ON)}$ for each MOSFET is approximately one-third the resistance of a single turn of a single strand in one of the stator coils. The switch can be controlled using digital outputs or PWM to create a resistance profile.

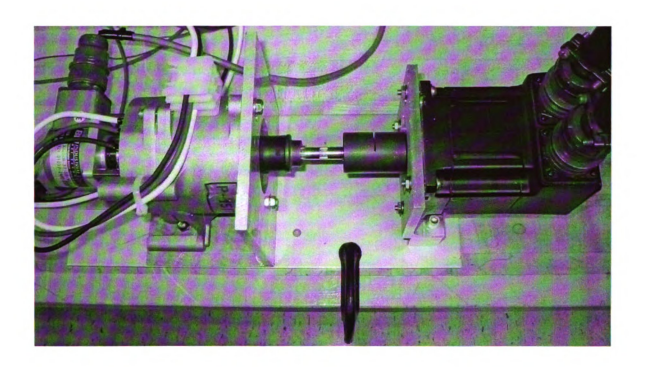


Figure 5.3. Motor / Dynamometer / Encoder Fixture

5.1 Experiment Fixture

A fixture and shaft coupling were built to couple the test motor, the dynamometer, and the encoder. The fixture is made from aluminum and allows for quick replacement of the test motor. This fixture was used for the electrical faults in this work and is shown in Fig. 5.3.

A custom shaft coupling was built for use between the test motor and the dynamometer. The flexible coupling and spline shaft from the gear reduction mechanism which the motor is coupled to are used, with the spline shaft cut to length for this application. The spline shaft is attached to a solid coupling with a 14 mm. bore for the spline shaft and a 1/2 in. bore for the dynamometer. Machining was required to create the 14 mm. bore in the solid coupling, since this bore combination was not available. The shaft coupling is shown in Fig. 5.4.

For the most recent experiments, with faster controller response, a solid coupling



Figure 5.4. Motor / Dynamometer Shaft Coupling

was fabricated for use between the test motor and the dynamometer. While the flexible coupling is used in the intended application for the motor, the solid coupling allows for the analysis of high frequency load-based faults originating from dynamometer or the mechanical gearbox used in this work. These high frequency phenomena are normally damped with the flexible coupling. The solid coupling is shown in Fig. 5.5.

Finally, a flexible shaft coupling was used between the test motor and the encoder.

An adapter plate was built to compensate for the differences in the bolt pattern on the encoder and on the back of the test motor. The magnetic disk used in the position sensor on the test motor must be removed for installation of the encoder.

The interface between the test motor and the encoder is shown in Fig. 5.6.

A second fixture, which added a mechanical gearbox to the setup described above, was built for the mechanical gear faults in this work. This fixture is shown in Fig. 5.7.



Figure 5.5. Motor / Dynamometer Solid Shaft Coupling



Figure 5.6. Motor / Encoder Interface

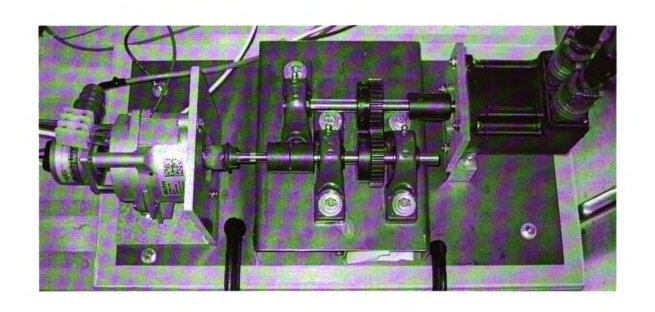


Figure 5.7. Mechanical Gearbox Experimental Setup

5.2 Xilinx I/O Board

The data acquisition board which is used in conjunction with the Xilinx FPGA board is used to receive phase and DC link currents, line-to-line and DC link voltages, and encoder position. The board is also used to send PWM signals to the gate drive chip on the motor controller, analog outputs to control the dynamometer, and digital outputs to control the electronic switch board. A listing of the available I/O follows:

• Inputs

- \circ 12 A/D channels (12-bit, ± 10 V single-ended or ± 5 V differential)
- $\circ\,$ 1 Quadrature encoder (differential or single-ended)

Outputs

- o 4 D/A channels (0-10V, 12-bit)
- o 12 PWM (or digital)

Bidirectional

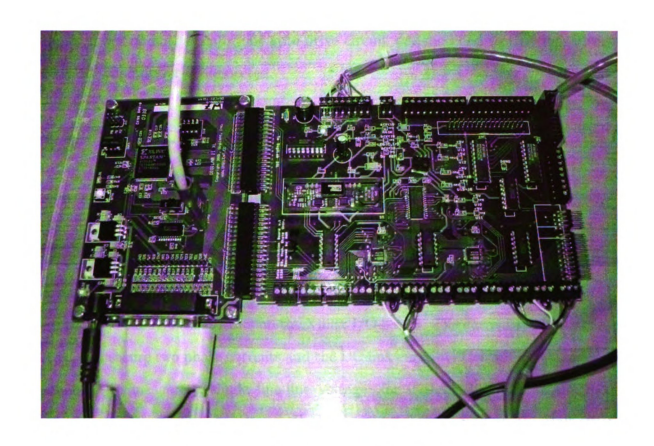


Figure 5.8. Xilinx and Xilinx I/O Boards

o 16 Digital (configurable as input or output in groups of 8)

The Xilinx I/O board along with the Xilinx board are shown in Fig. 5.8.

5.2.1 Inverter

A 12V, DSP-based, PMAC motor controller used for an automotive application was modified for use in this project. Sinusoidal PWM was used with 2500 counts of resolution at 20kHz. To facilitate control using RT-Linux, the DSP was removed from the board and connections were added for communication with the gate drive circuit directly. Modifications were also required in the input power circuit. Specifically, the DC link capacitor charging circuit was modified so that the capacitors always charge when power is connected and a switch was added to manually control the relay in the

input power circuit. Finally, the gate drive circuit was modified so that it is always enabled when power is connected.

5.3 Sensor Board

The sensor board consists of three current transducers and two voltage transducers. The current transducers are LEM model LA 100-P, and the voltage transducers are LEM model LV 25-P. The current transducers are configured to convert $\pm 133.33A$ to $\pm 10.0V$ and the voltage transducers are configured to convert $\pm 22.56V$ to $\pm 10.0V$ for input to the A/D converters on the Xilinx I/O board. The current transducers are used to measure two phase currents and the DC link current. The voltage transducers are used to measure a single line-line voltage (for initial calibration of the rotor position) and the DC link voltage. Both sensor types are based on the Hall effect. The sensor board is shown in Fig. 5.9.

5.4 Shaft Encoder

The encoder has dual quadrature channels, index pulse, 1024 counts per revolution (4096 for quadrature), and complementary outputs. The index pulse is used to reset the counter on the Xilinx board. Communication with the Xilinx I/O board uses the differential outputs to reduce noise.

5.5 Dynamometer

A PMAC dynamometer is used in this work to control the speed of the test machine. It is controlled by an analog command sent from the Xilinx I/O board which can be configured to be proportional to either torque or speed. The drive is Pacific Scientific model SC933. The motor is Pacific Scientific model S31H and has a sinusoidal back-

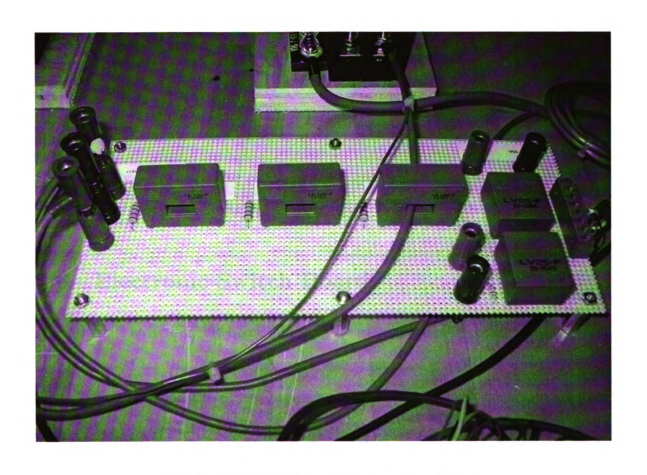


Figure 5.9. Current and Voltage Sensor Board

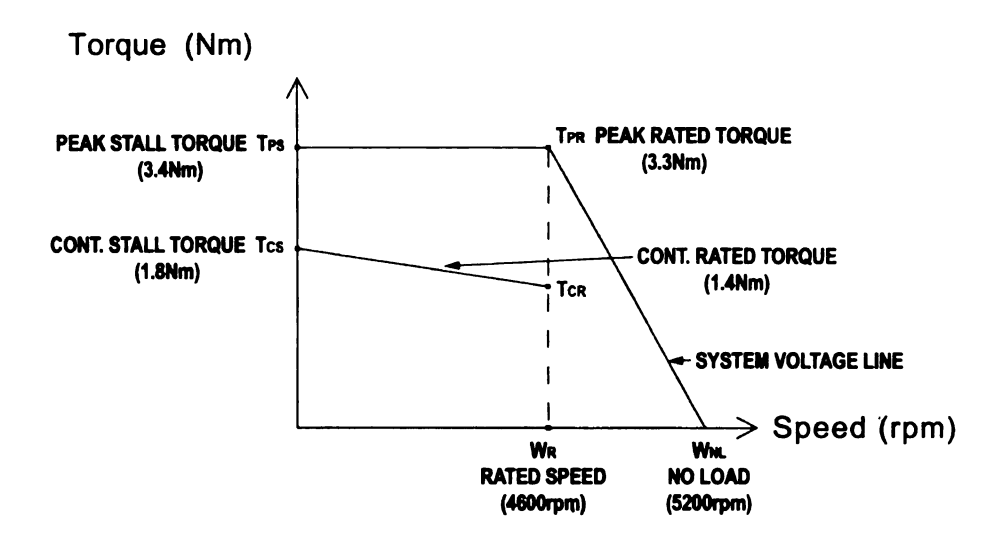


Figure 5.10. Dynamometer Torque-Speed Characteristics

EMF. The torque-speed curve of the motor is shown in Fig. 5.10. Additionally, the inertia of the motor $J = 0.18 kgm^2 \times 10^{-3}$.

5.6 Electronic Switch Board

An electronic switch circuit board allowing for several operating states was designed and fabricated for this work. The circuit has three analog switches; one provides a direct connection and the others have an additional series resistance, e.g. 1Ω , and 50Ω . Either one or both resistances can be enabled simultaneously. The switches can be controlled using digital inputs or PWM to create a resistance profile to simulate turn to turn insulation failures. Since the switches are floating, they have isolated gate drives and power supplies. The schematic and layout for the board are shown in Figs. 5.11 and 5.12 respectively. The board was fabricated using a machining process on a two-sided, 4oz. copper per square ft., 1/16 in. thick, FR4 board.

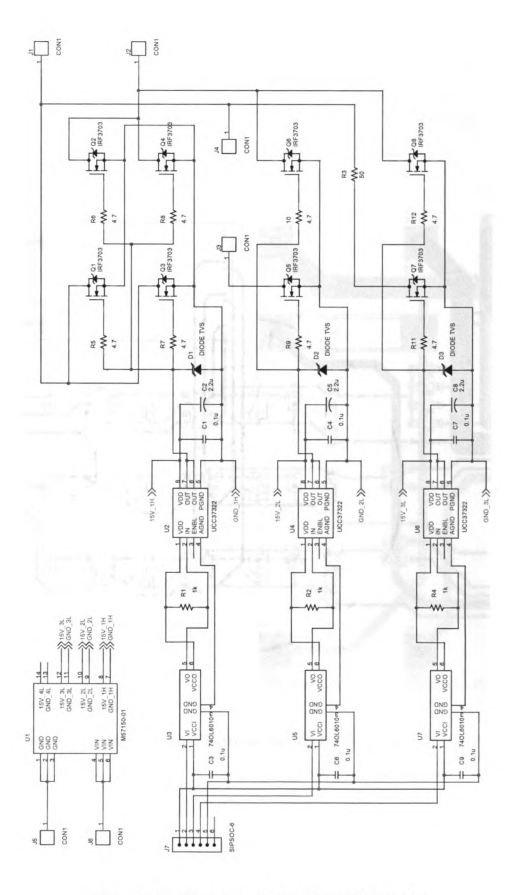


Figure 5.11. Electronic Switch Board Schematic

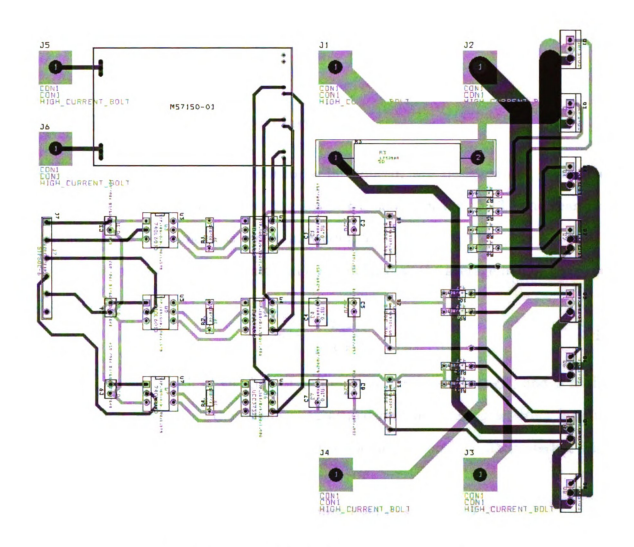


Figure 5.12. Electronic Switch Board Layout

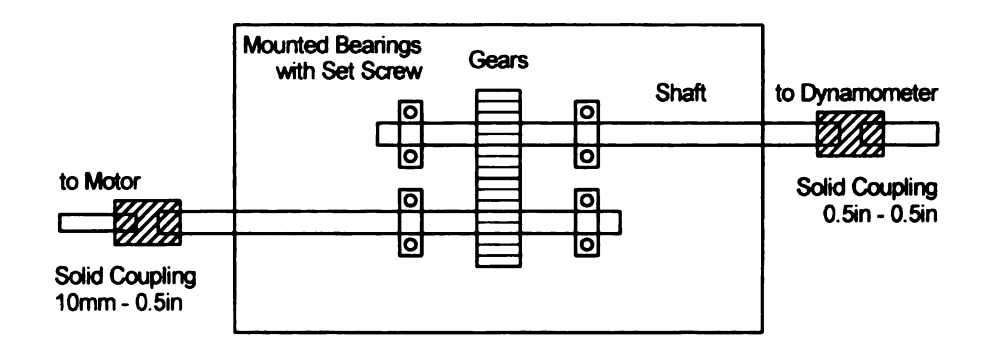


Figure 5.13. Gear Box Block Diagram

5.7 Mechanical Gearbox

A gearbox, allowing for gear faults to be introduced, was designed and fabricated for this work. A block diagram of the gearbox is shown in Fig. 5.13. The gearbox, installed in the experiment, is shown in Section 5.1.

The design specifies the contact ratio, m_c , defined as the average number of pairs of teeth in contact (5.1),

$$m_c = \frac{L_{ab}}{p \cdot \cos \phi} \tag{5.1}$$

where L_{ab} is the length of the line of action, ϕ is the pressure angle, and p is the circular pitch, defined as the distance, measured on the pitch circle, from a point on one tooth to a corresponding point on an adjacent tooth as illustrated in Fig. 5.14 [51].

To determine L_{ab} , the Law of Sines is first used to solve for β (5.2).

$$\frac{\sin(90 - \phi)}{a} = \frac{\sin \beta}{\text{pitch}}$$

$$\beta = \arcsin\left(\frac{\text{pitch} \cdot \sin(90 - \phi)}{a}\right)$$
(5.2)

Then γ can be determined (5.3).

$$\gamma = 90 + \phi - \beta \tag{5.3}$$

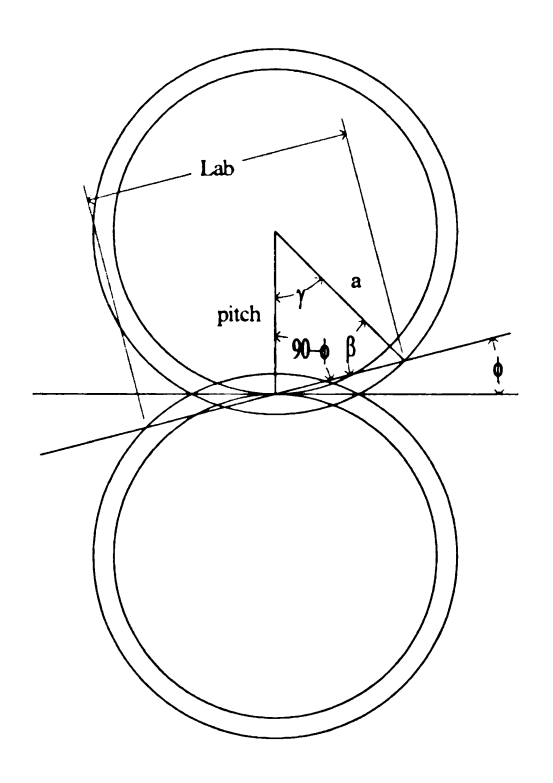


Figure 5.14. Gear Illustration

Finally, the Law of Sines is applied again to determine $L_{ab}(5.4)$.

$$\frac{\sin(90 - \phi)}{a} = \frac{\sin \gamma}{L_{ab}/2}$$

$$L_{ab} = \frac{2a \cdot \sin(90 + \phi - \beta)}{\sin(90 - \phi)}$$
(5.4)

For $m_c \approx 8$, the following gear parameters were specified: Pressure angle=14.5°; number of teeth=36; pitch diameter=2.25"; outer diameter=2.38"; and bore=0.5". The resultant value of m_c was 8.007.

CHAPTER 6

Conclusions

Algorithms capable of identifying intermittent electrical and mechanical faults in PMAC drives have been developed. They can be used to give a prognosis for failure of a drive. They are based on the detection and classification of small transients in the stator currents corresponding to non-catastrophic faults.

Unlike prior methods, the methods proposed here are capable of recognizing steady fault conditions as well as the transient phenomena associated with intermittent faults which can develop into a catastrophic fault, and evaluating their severity and frequency. Early detection of these faults can give indication when maintenance or mitigation is required, minimizing the likelihood of system failure. This work addresses the limitation of existing methods which can only detect permanent faults in drives.

The UDWT, as used in this work, is shift-invariant and offers good time resolution of high frequency components and good time and frequency resolution of low frequency components in the same analysis. The UDWT allows for increased flexibility and resolution when compared to the more traditional FFT and STFT, and overcomes the drawbacks of the DWT. This method is unique in overcoming the non-shift-invariant nature of Fourier and standard wavelet methods.

The categorization algorithm uses a linear discriminant function and is trained

using a set of operating conditions, which include healthy drives and samples of faulted drives. An exhaustive set of such conditions is necessary to develop a robust algorithm.

Although the algorithms in this work were used offline, they can be added to an existing motor controller, enabling them to run close to real-time. The vector current of the stator needed is typically calculated as part of the standard drive control. Minimal, if any, additional CPU speed and memory capacity would be required ensuring a low-cost system. The training phase of the algorithms would remain offline.

Some of the topics in this work could be further explored in future research: Testing the algorithms developed using varying speeds and loads in the drive; optimization of the STFT window type, length, and sampling frequency; optimization of the UDWT mother wavelet, number of scales, and sampling frequency; elimination of uninteresting parameters in the pattern recognition algorithm resulting in reduced complexity; and identification of faults using the DC link current rather than the field oriented currents calculated using two measured phase currents.

BIBLIOGRAPHY

BIBLIOGRAPHY

- [1] A. Cash, T. G. Habetler, and G. B. Kliman, "Insulation Failure Prediction in AC Machines Using Line-Neutral Voltages," *IEEE Transactions on Industry Applications*, vol. 34, pp. 1234–1239, Nov–Dec 1998.
- [2] H. Nejjari and M. E. Benbouzid, "Monitoring and Diagnosis of Induction Motors Electrical Faults Using a Current Park's Vector Pattern Learning Approach," *IEEE Transactions on Industry Applications*, vol. 36, pp. 730–735, May–Jun 2000.
- [3] A. Bellini, F. Filippetti, G. Franceschini, C. Tassoni, R. Passaglia, M. Saottini, G. Tontini, M. Giovannini, and A. Rossi, "On-Field Experience With Online Diagnosis of Large Induction Motors Cage Failures using MSCA," *IEEE Transactions on Industry Applications*, vol. 38, pp. 1045–1053, Jul–Aug 2002.
- [4] C. C. Yeh, B. Mirafzal, R. J. Povinelli, and N. A. O. Demerdash, "A condition monitoring vector database approach for broken bar fault diagnostics of induction machines," in *International Electric Machines and Drives Conference*, pp. 29–34, May 2005.
- [5] O. Moseler and R. Isermann, "Application of Model-Based Fault Detection to a Brushless DC Motor," *IEEE Transactions on Industrial Electronics*, vol. 47, pp. 1015–1020, Oct 2000.
- [6] X. Q. Liu, H. Y. Zhang, J. Liu, and J. Yang, "Fault Detection and Diagnosis of Permanent-Magnet DC Motor Based on Parameter Estimation and Neural Network," *IEEE Transactions on Industrial Electronics*, vol. 47, pp. 1021–1030, Oct 2000.
- [7] A. R. Webb, Statistical Pattern Recognition. John Wiley & Sons, 2nd ed., 2002.
- [8] S. Pöyhönen, M. Negrea, P. Jover, A. Arkkio, and H. Hyötyniemi, "Numerical Magnetic Field Analysis and Signal Processing for Fault Diagnostics of Electrical Machines," in *International Conference on Electrical Machines*, Aug 2002.

- [9] M. Dai, A. Keyhani, and T. Sebastian, "Fault Analysis of a Trapezoidal Back-EMF Permanent Magnet Brushless DC Motor Using Finite Element Method," *IEEE Transactions on Energy Conversion*, 2001 (in print).
- [10] N. Bianchi, S. Bolognani, and M. Zigliotto, "Analysis of PM Synchronous Motor Drive Failures During Flux Weakening Operation," in 27th Annual IEEE Power Electronics Specialists Conference, vol. 2, pp. 1542-1548, Jun 1996.
- [11] C. Combastel, S. Lesecq, S. Petropol, and S. Gentil, "Model-Based and Wavelet Approaches to Induction Motor On-Line Fault Detection," *Control Engineering Practice*, vol. 10, pp. 493–509, May 2002.
- [12] B. A. Paya, I. I. Esat, and M. N. M. Badi, "Artificial Neural Network Based Fault Diagnostics of Rotating Machinery Using Wavelet Transforms as a Preprocessor," *Mechanical Systems and Signal Processing*, vol. 11, pp. 751–765, Sep 1997.
- [13] W. le Roux, R. G. Harley, and T. G. Habetler, "Rotor Fault Analysis of a Permanent Magnet Synchronous Machine," *International Conference on Electrical Machines*, 2002.
- [14] W. J. Wang, "Wavelets for Detecting Mechanical Faults with High Sensitivity," *Mechanical Systems and Signal Processing*, vol. 15, pp. 685-696, Jul 2001.
- [15] C. W. Cheng, M. C. Tsai, and M. Y. Cheng, "Fault Detection for Servomechanisms using the Load Torque Observer and Discrete Wavelet Transform," in Proceedings of the 7th International Conference on Mechatronics Technology, pp. 157-162, 2003.
- [16] H. S. Liu, B. Y. Lee, and Y. S. Tarng, "Monitoring of Drill Fracture from the Current Measurement of a Three-Phase Induction Motor," *International Journal* of Machine Tools and Manufacture, vol. 36, pp. 729–738, Jun 1996.
- [17] J. Altmann and J. Mathew, "Multiple Band-Pass Autoregressive Demodulation for Rolling-Element Bearing Fault Diagnosis," *Mechanical Systems and Signal Processing*, vol. 15, pp. 963–977, Sep 2001.
- [18] R. B. Randall, J. Antoni, and S. Chobsaard, "The Relationship between Spectral Correlation and Envelope Analysis in the Diagnostics of Bearing Faults and other Cyclostationary Machine Signals," *Mechanical Systems and Signal Processing*, vol. 15, pp. 945–962, Sep 2001.

- [19] D. M. Yang, A. F. Stronach, P. MacConnell, and J. Penman, "Third-Order Spectral Techniques for the Diagnosis of Motor Bearing Condition using Artificial Neural Networks," *Mechanical Systems and Signal Processing*, vol. 16, pp. 391–411, Mar-May 2002.
- [20] A. Belšak, M. P. Virtič, B. Aberšek, and J. Flašker, "Vibrations Diagnostics of a Gear Unit," *Key Engineering Materials*, vol. 251–252, pp. 457–462, 2003.
- [21] I. Yesilyurt, "The Application of the Conditional Moments Analysis to Gearbox Fault Detection a Comparative Study Using the Spectrogram and Scalogram," NDT & International, vol. 37, pp. 309–320, Jun 2004.
- [22] H. Zheng, Z. Li, and X. Chen, "Gear Fault Diagnosis based on Continuous Wavelet Transform," Mechanical Systems and Signal Processing, vol. 16, pp. 447–457, Mar–May 2002.
- [23] W. G. Zanardelli, E. G. Strangas, H. K. Khalil, and J. M. Miller, "Wavelet-Based Methods for the Prognosis of Mechanical and Electrical Failures in Electric Motors," *Mechanical Systems and Signal Processing*, pp. 411–426, Mar 2005.
- [24] W. G. Zanardelli, E. G. Strangas, H. K. Khalil, and J. M. Miller, "Comparison of Wavelet-Based Methods for the Prognosis of Failures in Electric Motors," *IEEE Workshop on Power Electronics in Transportation*, pp. 61–67, 2002.
- [25] W. G. Zanardelli, E. G. Strangas, H. K. Khalil, and J. M. Miller, "The Use of Wavelet Analysis and the Nearest Neighbor Rule for the Prognosis of Failures in Electric Motors," *IEEE International Symposium on Diagnostics for Electrical Machines, Power Electronics and Drives*, pp. 591–596, Sep 2001.
- [26] W. G. Zanardelli, "The Use of Wavelet Analysis for the Prognosis of Failures in Electric Motors," Master's thesis, Michigan State University, 2000.
- [27] R. R. Schoen, T. G. Habetler, F. Kamran, and R. G. Bartheld, "Motor Bearing Damage Detection Using Stator Current Monitoring," *IEEE Transactions on Industry Applications*, vol. 31, pp. 1274–1279, Nov-Dec 1995.
- [28] R. R. Schoen, B. K. Lin, T. G. Habetler, J. H. Schlag, and S. Farag, "An Unsupervised, On-Line System for Induction Motor Fault Detection Using Stator Current Monitoring," *IEEE Transactions on Industry Applications*, vol. 31, pp. 1280–1286, Nov-Dec 1995.

- [29] S. F. Farag, R. G. Bartheld, and T. G. Habetler, "An Integrated On-Line Motor Protection System," *IEEE Industry Applications Magazine*, vol. 2, pp. 21–26, Mar-Apr 1996.
- [30] C. Kim, H. Kim, Y. Ko, S. Byun, R. K. Aggarwal, and A. T. Johns, "A Novel Fault-Detection Technique of High-Impedence Arcing Faults in Transmission Lines Using the Wavelet Transform," *IEEE Transactions on Power Delivery*, vol. 17, pp. 921–929, Oct 2002.
- [31] T. S. Sidhu, G. S. Sagoo, and M. S. Sachdev, "On-Line Detection and Location of Low-Level Arcing in Dry-Type Transformers," *IEEE Transactions on Power Delivery*, vol. 16, pp. 135–141, Jan 2002.
- [32] B. A. Welchko, T. A. Lipo, T. M. Jahns, and S. E. Schulz, "Fault Tolerant Three-Phase AC Motor Drive Topologies; A Comparison of Features, Cost, and Limitations," in *IEEE International Electric Machines and Drives Conference*, vol. 1, pp. 539–546, Jun 2003.
- [33] D. Kastha and B. K. Bose, "Fault Mode Single-Phase Operation of a Variable Frequency Induction Motor Drive and Improvement of Pulsating Torque Characteristics," *IEEE Transactions on Industrial Electronics*, vol. 41, pp. 426–433, Aug 1994.
- [34] L. Cohen, Time-Frequency Analysis. Prentice Hall, 1995.
- [35] C. S. Burrus, R. A. Gopinath, and H. Guo, Introduction to Wavelets and Wavelet Transforms, A Primer. Prentice Hall, 1998.
- [36] S. Mallat, A Wavelet Tour of Signal Processing. Academic Press, 2nd ed., 1999.
- [37] P. Dutilleux, "An Implementation of the "algorithme à trous" to Compute the Wavelet Transform," in Wavelets: Time-Frequency Methods and Phase Space, Proceedings of the International Conference, Springer-Verlag, 1987.
- [38] W. J. Williams, E. J. Zalubas, and A. O. Hero, III, "Word Spotting in Bitmapped Fax Documents," *Information Retrieval*, vol. 2, pp. 207–226, May 2000.
- [39] L. Cohen, "The Scale Representation," *IEEE Transactions on Signal Processing*, vol. 41, pp. 3275–3292, Dec 1993.
- [40] W. J. Williams, E. J. Zalubas, and A. O. Hero, III, "Separating Desired Image and Signal Invariant Components from Extraneous Variations," SPIE: Advanced

- Signal Processing Algorithms, Architectures, and Implementations, vol. 2846, pp. 262–272, Oct 1996.
- [41] T. M. Cover and P. E. Hart, "Nearest Neighbor Pattern Classification," *IEEE Transactions on Information Theory*, vol. IT-13, no. 1, pp. 21–27, 1967.
- [42] J. H. Friedman, F. Baskett, and L. J. Shustek, "An Algorithm for Finding Nearest Neighbors," *IEEE Transactions on Computers*, pp. 1000-1006, Oct 1975.
- [43] T. Y. Young and T. W. Calvert, Classification, Estimation and Pattern Recognition. American Elsevier Publishing Co., Inc., 1974.
- [44] B. Efron and G. Gong, "A Leisurely Look at the Bootstrap, the Jackknife, and Cross-Validation," *The American Statistician*, vol. 37, pp. 36–48, Feb 1983.
- [45] R. Krishnan, Electric Motor Drives: Modeling, Analysis, and Control. Prentice Hall, 2001.
- [46] J. D. Neely, "Fault Types and Reliability Estimates in Permanent Magnet AC Motors," Master's thesis, Michigan State University, 2005.
- [47] W. G. Zanardelli and E. G. Strangas, "Failure Prognosis for Permanent Magnet AC Machines Based on Time-Frequency Analysis," *International Conference on Electrical Machines*, Sep 2004.
- [48] W. G. Zanardelli, E. G. Strangas, and S. Aviyente, "Intermittent Fault Identification for Permanent Magnet AC Drives Based on the Short-Time Fourier Transform," *IEEE International Symposium on Diagnostics for Electrical Machines, Power Electronics and Drives*, pp. 3–8, Sep 2005.
- [49] W. G. Zanardelli and E. G. Strangas, "Methods to Identify Intermittent Electrical and Mechanical Faults in Permanent Magnet AC Drives Based on Wavelet Analysis," IEEE Vehicle Power and Propulsion Conference, pp. 154–160, Sep 2005.
- [50] W. G. Zanardelli, E. G. Strangas, and S. Aviyente, "Failure prognosis for permanent magnet AC drives based on wavelet analysis," in *International Electric Machines and Drives Conference*, pp. 64–70, May 2005.
- [51] J. E. Shigley and C. R. Mischke, *Mechanical Engineering Design*. McGraw-Hill, 6th ed., 2001.

